The impact of stellar feedback on the density and velocity structure of the interstellar medium

Kearn Grisdale,[1][*] Oscar Agertz,[1,2] Alessandro B. Romeo,[3] Florent Renaud[1] and Justin I. Read[1]

[1]*Department of Physics, University of Surrey, Guildford GU2 7XH, UK*
[2]*Lund Observatory, Department of Astronomy and Theoretical Physics, Lund University, Box 43, SE-221 00 Lund, Sweden*
[3]*Department of Earth and Space Sciences, Chalmers University of Technology, SE-41296 Gothenburg, Sweden*

ABSTRACT

We study the impact of stellar feedback in shaping the density and velocity structure of neutral hydrogen (H I) in disc galaxies. For our analysis, we carry out $\sim$4.6 pc resolution N-body+adaptive mesh refinement hydrodynamic simulations of isolated galaxies, set up to mimic a Milky Way and a Large and Small Magellanic Cloud. We quantify the density and velocity structure of the interstellar medium using power spectra and compare the simulated galaxies to observed H I in local spiral galaxies from THINGS (The H I Nearby Galaxy Survey). Our models with stellar feedback give an excellent match to the observed THINGS H I density power spectra. We find that kinetic energy power spectra in feedback-regulated galaxies, regardless of galaxy mass and size, show scalings in excellent agreement with supersonic turbulence ($E(k) \propto k^{-2}$) on scales below the thickness of the H I layer. We show that feedback influences the gas density field, and drives gas turbulence, up to large (kpc) scales. This is in stark contrast to density fields generated by large-scale gravity-only driven turbulence. We conclude that the neutral gas content of galaxies carries signatures of stellar feedback on all scales.

Key words: galaxies: evolution – galaxies: ISM – galaxies: spiral – galaxies: structure.

1 INTRODUCTION

Galaxy formation is an inefficient process. Different methods such as abundance matching (Tasitsiomi et al. 2004; Vale & Ostriker 2004; Read & Trentham 2005; Kravtsov, Vikhlinin & Meshscheryakov 2014), satellite kinematics (Klypin & Prada 2009; More et al. 2011) and weak lensing (Mandelbaum et al. 2006) all indicate that a surprisingly low fraction of cosmic baryons tend up as stars in the centres of dark matter haloes, with stellar-to-dark matter mass fractions of $M_\star/M_{\rm h} \approx$ 3–5 per cent for $L_\star$ galaxies, well below the cosmological baryon fraction of $\Omega_{\rm b}/\Omega_{\rm m} \approx 16$ per cent (Planck Collaboration XIII 2016). For both less and more massive galaxies, $M_\star/M_{\rm h}$ is even lower.

Such low baryon fractions are believed to be due to galactic winds driven by stellar feedback (e.g. radiative feedback, supernovae, stellar winds, cosmic rays, etc.) at the faint end of the stellar mass function (Dekel & Silk 1986; Efstathiou 2000) and by the active galactic nuclei and the bright end (Silk & Rees 1998; Benson et al. 2003). Over the last two decades, there has been a significant effort to model these processes in simulations of galaxy formation

and evolution (e.g. Katz 1992; Navarro & White 1993; Thacker & Couchman 2001; Stinson et al. 2006; Avila-Reese et al. 2011; Hopkins et al. 2014; Agertz & Kravtsov 2015; Kimm et al. 2015). However, stellar feedback has proven to be challenging to simulate, and results are generally mixed, as many processes are still poorly understood, e.g. the efficacy of radiative feedback for galactic wind driving. No consensus yet exists on exactly which feedback processes are crucial to model. At a spatial resolution of $\sim$500 pc, Scannapieco et al. (2012) show that, for Milky Way-mass galaxies, the details of the algorithmic implementations of stellar feedback significantly influence the resulting galaxies. However, higher resolution simulations that reach spatial scales of $\lesssim$100 pc and begin to resolve the multiphase interstellar medium (ISM) are in much better agreement (e.g. Kravtsov 2003; Stinson et al. 2013; Hopkins et al. 2014; Agertz & Kravtsov 2016; Read et al. 2016b,c). These simulations find that stellar feedback allows galaxy formation simulations to reproduce not only the stellar mass–halo mass relation, but also the evolution of basic properties of spiral galaxies: stellar mass, disc size, morphology dominated by a kinematically cold disc, stellar and gas surface density profiles, and specific angular momentum.

Given the improvement in spatial resolution, with many authors now reporting sub-100 pc resolution in a cosmological context

[*]E-mail: k.grisdale@surrey.ac.uk

(e.g. Hopkins et al. 2014; Agertz & Kravtsov 2015, 2016), and even higher resolution for isolated galaxy simulations (e.g. Renaud et al. 2013; Read et al. 2016c), this opens up the possibility of studying the role of feedback by not only considering integral properties of galaxies such as size and mass, but by using detailed observations of the structure of neutral gas in nearby galaxies (e.g. Walker et al. 2014).

Today, decades after the pioneering work by Larson (1981), observations and simulations of the ISM are revealing its turbulent nature with higher and higher fidelity (see review by e.g. Elmegreen & Scalo 2004; Mac Low & Klessen 2004). H I emission lines in most spiral galaxies have characteristic velocity dispersions of $\sigma \sim 10\,\mathrm{km\,s^{-1}}$ on a scale of a few hundred parsecs (Tamburro et al. 2009), exceeding the values expected from purely thermal effects. This suggests that the ISM is *supersonically* turbulent. Turbulence controls the overall structure of the ISM, and is an important ingredient for star formation (McKee & Ostriker 2007), not only for determining the rate of star formation in molecular clouds (Federrath & Klessen 2012; Padoan et al. 2014), but also by affecting the global and local stability properties of galaxies (Romeo, Burkert & Agertz 2010; Hoffmann & Romeo 2012; Romeo & Agertz 2014; Agertz, Romeo & Grisdale 2015).

The structure of the ISM has been studied using numerical simulations of isolated models of galaxies (e.g. Tasker & Bryan 2006; Agertz et al. 2009; Dobbs, Burkert & Pringle 2011; Hopkins, Quataert & Murray 2012; Renaud et al. 2013; Marasco et al. 2015), as well as individual patches of the ISM (Joung & Mac Low 2006; Gatto et al. 2015; Martizzi, Faucher-Giguere & Quataert 2015; Walch et al. 2015). The main sources of turbulence driving are still not clear. Several candidates capable of driving the ISM turbulence exist, for example large-scale expanding outflows from high-pressure H II regions (Kessel-Deynet & Burkert 2003), stellar winds or supernovae (SNe; e.g. Kim, Balsara & Mac Low 2001; de Avillez & Breitschwerdt 2004, 2005; Joung & Mac Low 2006), gravitational instabilities coupled with galactic rotation (Gammie, Ostriker & Jog 1991; Piontek & Ostriker 2004; Ibáñez-Mejía et al. 2016; Krumholz & Burkhart 2016) and the magnetorotational instability (Balbus & Hawley 1991), to name a few.

The turbulent ISM is often conveniently characterized in Fourier space using power spectra. Kolmogorov (1941) proved that incompressible turbulence will feature an energy spectrum $E(k) \propto k^{-5/3}$ below the injection scale, where $k \propto 1/\ell$ is the wavenumber and ℓ the physical scale. Supersonically turbulent gas features a steeper spectrum, with $E(k) \propto k^{-2}$ (Burgers 1948), as conformed by idealized numerical simulations of turbulent gas (e.g. Kritsuk et al. 2007a). On galactic scales, simulations indicate that turbulent scalings are present (e.g. Wada, Meurer & Norman 2002; Agertz et al. 2015), but as mentioned above, it is not established which physical mechanisms are required to maintain them, and whether the observed H I content of galaxies features the same energetics as idealized galaxy simulations. Observations of the neutral ISM in nearby galaxies have revealed that the H I component often gives rise to simple power-law behaviours ($P(k) \propto k^{-\alpha}$), with α typically in the range 1–3, over several orders of magnitude in scale (e.g. Stanimirovic et al. 1999; Bournaud et al. 2010; Combes et al. 2012; Zhang, Hunter & Elmegreen 2012; Dutta et al. 2013). This points towards the presence of turbulence. Broken power laws are also observed, possibly owing to the finite thickness of the disc causing a transition from 2D turbulence on large scales to 3D turbulence on small scales (for example, see NGC 1058 in Dutta et al. 2009b).

This leads us to the main question that we seek to answer in this work: what are the observational signatures of stellar feedback on

the galactic density and velocity structure of H I gas, from small ($\sim$10 pc) to large ($>$kpc) scales, and can these be used to discriminate between sources of turbulence? To address this question, we perform hydrodynamical simulations of disc galaxies of varying sizes and masses (thus giving different star formation rates and therefore different feedback injection rates) and compare these to observations of the cold ISM in nearby galaxies. Our goal is to understand the role of stellar feedback in shaping the density and velocity structure of the ISM.

The paper is organized as follows. In Section 2, we describe the numerical method, the observational data, as well as the adopted power spectrum analysis method. In Section 3, we present power spectra of the simulated density and energy field and compare these to the observed neutral ISM in nearby spiral galaxies. We discuss our findings in Section 4 and investigate existing uncertainties in simulations and observations. Furthermore, we relate our results to the literature. Finally, in Section 5 we present our conclusions.

2 METHOD

2.1 Numerical technique

We use the adaptive mesh refinement (AMR) code RAMSES (Teyssier 2002) to carry out hydro+N-body simulations of galactic discs for comparison with observations. The fluid dynamics of the baryons is calculated using a second-order unsplit Godunov method, while the collisionless dynamics of stellar and dark matter particles is evolved using the particle-mesh technique (Hockney & Eastwood 1981), with gravitational accelerations computed from the gravitational potential on the mesh. The gravitational potential is calculated by solving the Poisson equation using the multi-grid method (Guillet & Teyssier 2011) for all refinement levels. The equation of state of the fluid is that of an ideal mono-atomic gas with an adiabatic index $\gamma = 5/3$.

The code achieves high resolution in high-density regions using AMR, where the refinement strategy is based on a quasi-Lagrangian approach in which the number of collisionless particles per cell is kept approximately constant at 8. This allows the local force softening to closely match the local mean inter-particle separation, which suppress discreteness effects (e.g. Romeo et al. 2008). In addition to this, cell refinement is triggered when the baryonic mass (stars and gas) in a cell exceeds a fixed threshold M_{ref}, see Section 2.2.

The star formation, cooling physics and stellar feedback model adopted in our simulations is identical to the implementation used in Agertz et al et al. (2015), and described in detail in Agertz et al. (2013) and Agertz & Kravtsov (2015, see also Read, Agertz & Collins 2016a; Read et al. 2016c). We refer the reader to those papers for details. Briefly, we model the local star formation rate (SFR) using the following equation,

$$\dot{\rho}_\star = f_{\mathrm{H}_2} \frac{\rho_{\mathrm{g}}}{t_{\mathrm{SF}}}, \tag{1}$$

where f_{H_2} is the local mass fraction of molecular hydrogen (H$_2$), ρ_{g} is the gas density in a cell and t_{SF} is the star formation time-scale of *molecular* gas. The fraction of molecular hydrogen in a cell is a function of the gas density and metallicity and is computed using the KMT09 model (Krumholz, McKee & Tumlinson 2008, 2009) that implemented as described in Agertz & Kravtsov (2015, see their section 2.3, equations 2–6).

The star formation time-scale is related to the *local* efficiency of star formation in a computational cell of a given density as

Table 1. Initial conditions of simulated galaxies. Column 1: name of simulation, column 2: stellar mass of the disc, column 3: stellar mass of the galactic bulge, column 4: mass of dark matter halo, column 5: gas-to-stellar mass ($M_{\mathrm{gas, disc}}/M_{\star, \mathrm{total}}$), column 6: gas scalelength of the disc, column 7: gas scaleheight of disc, column 8: gas scale radius of galactic bugle, column 9: rotational velocity at r_{200}, column 10: concentration parameter and column 11: gas metallicity as a function of solar metallicity.

Simulation	Stellar disc mass (10^8 M$_\odot$)	Stellar bulge mass (10^8 M$_\odot$)	Dark matter halo mass (10^{10} M$_\odot$)	Gas fraction	Scalelength (kpc)	Scaleheight (kpc)	Bulge scalelength (kpc)	v_{200} (km s^{-1})	c	Gas metallicity (Z$_\odot$)
MW	343.7	43.0	125.4	0.20	3.43	0.34	0.3432	150	10	1.75
LMC	21.8	0.035	21.28	0.38	3.35	0.34	0.0167	82	9	0.53
SMC	1.1	0.005	2.59	0.90	1.16	0.12	0.0058	42	15	0.18

$t_{\mathrm{SF}} = t_{\mathrm{ff, SF}}/\epsilon_{\mathrm{ff, SF}}$, where $t_{\mathrm{ff,SF}} = \sqrt{3\pi/32G\rho_{\mathrm{g}}}$ is the local free-fall time of the star-forming gas and $\epsilon_{\mathrm{ff, SF}}$ is the local star formation efficiency per free-fall time. We adopt $\epsilon_{\mathrm{ff, SF}} = 1\text{--}10$ per cent in this work, see Section 2.2. In every cell, equation (1) is sampled using a Poisson process (see e.g. Dubois & Teyssier 2008), where resulting star particles are assumed to have an internal stellar mass distribution according to a Chabrier (2003) initial mass function. At the time of formation, star particles have an initial mass of 300 M$_\odot$, and can lose up to ∼40 per cent of their mass over a Hubble time due to stellar evolution processes.

Several processes contribute to the stellar feedback budget, as stars inject energy, momentum, mass and heavy elements over time via SNII and SNIa explosions, stellar winds and radiation pressure into the surrounding gas. Metals injected by SNe and stellar winds are advected as a passive scalar and are incorporated self-consistently in the cooling and heating routine. Furthermore, we adopt the SN momentum injection model recently suggested by Kim & Ostriker (2015, see also Gatto et al. 2015; Martizzi et al. 2015; Simpson et al. 2015). Here we consider a SN explosion to be resolved when the cooling radius[1] is resolved by at least three grid cells ($r_{\mathrm{cool}} \geq 3\Delta x$). In this case, the explosion is initialized in the energy conserving phase by injecting the relevant energy (10^{51} erg per SN) into the nearest grid cell. If this criterion is not fulfilled, the SN is initialized in its momentum conserving phase, i.e. the total momentum generated during the energy conserving Sedov–Taylor phase is injected into the 26 cells surrounding a star particle. It can be shown (e.g. Blondin et al. 1998; Kim & Ostriker 2015) that at this time, the momentum of the expanding shell is approximately $p_{\mathrm{ST}} \approx 2.6 \times 10^5 \, E_{51}^{16/17} n_0^{-2/17}$ M$_\odot$ km s^{-1}.

2.2 Simulation suite

We run reference simulations, in which density and turbulence are set only by gravity and hydrodynamics (i.e. with no feedback regulation). We then quantify the effect of stellar feedback in shaping the ISM by running identical simulations including the stellar feedback model described above and compare the density and turbulence structures of the two sets of simulations.

We carry out numerical simulations of Milky Way (MW)-, Large Magellanic Cloud (LMC)- and Small Magellanic Cloud (SMC)-like galaxies. The characteristics of these galaxies are presented in Table 1. The initial conditions (ICs) feature a stellar disc, stellar bulge, gaseous disc and dark matter halo. We set up the particle distributions following the approach by Hernquist (1993) and Springel

(2000, Springel, Di Matteo & Hernquist 2005), assuming an exponential surface density profile for the disc, a Hernquist bulge density profile (Hernquist 1990) and an NFW dark matter halo profile (Navarro, Frenk & White 1996). We use 10^6 particles for both the NFW halo and stellar discs, with the same mass resolution in the bulge component as in the disc. We initialize the gaseous disc on the AMR grid assuming an exponential profile, and assume the galaxies to be embedded in a hot ($T = 10^6$ K), tenuous ($n = 10^{-5}$ cm^{-3}) corona enriched to $Z = 10^{-2}$ Z$_\odot$, while the discs have the abundances given in Table 1. All simulations include the same tenuous hot corona. Despite the temperature and density being reasonable for the MW (see Gatto et al. 2013), the corona in all simulations is unrealistic, for example the gas is not stratified. However, as the coronal mass is insignificant, and there is no significant accretion on to the discs, these corona models are sufficient for this work. Each galaxy is simulated in isolation, i.e. we neglect environmental effects such as galaxy interactions. The galaxies are set at the centre of a box with a size of $L_{\mathrm{box}} = 600$ kpc, and run with 17 levels of AMR, allowing for a finest grid cell size of $\Delta x \sim 4.6$ pc. The mass refinement threshold is $M_{\mathrm{ref}} \approx 9300$ M$_\odot$ for the MW simulations and $M_{\mathrm{ref}} \approx 930$ M$_\odot$ for LMC and SMC simulations, leading to baryon mass resolutions of just below ∼1200 and ∼120 M$_\odot$, respectively.

The MW models use the ICs from Agertz et al. (2013, the AGORA ICs, see also Kim, Abel & Agertz 2014). We generate the LMC and SMC ICs by applying the parametrization adopted by Mo, Mao & White (1998) using the following parameters from table 1 of Besla et al. (2010): concentration, gas fraction and V_{200} (the virial velocity, i.e. the circular velocity at the radius where the mean density of the dark matter halo is 200 times the critical density of the Universe). For both the LMC and SMC simulations, we employ a spin parameter $\lambda = 0.05$ (e.g. Bullock et al. 2001). We emphasize that these simulations are not designed to match the real galaxies; instead, we model spiral galaxies with similar gas fractions, stellar masses and dark matter halo masses as the MW, LMC and SMC. While the ICs employed for the LMC- and SMC-like simulations have stellar and gas masses consistent with observations of the LMC (Meatheringham et al. 1988; Kim et al. 1998; van der Marel et al. 2002) and SMC (Stanimirovic, Staveley-Smith & Jones 2004; Yozin & Bekki 2014), we note that the adopted scalelengths for the initial gas distributions are smaller than what is commonly derived from observations (see e.g. Besla et al. 2010, and references within).

We note that the MW analogue was designed to have characteristics of a typical Sb-Sbc galaxy in order to facilitate a comparison with the H I data in the THINGS (The H I Nearby Galaxy Survey) spiral galaxy sample, see Section 2.3. The LMC and SMC models allow us to study how the ISM is influenced by stellar feedback in low-mass galaxies, and will be compared both to previous numerical studies (e.g. Bournaud et al. 2010) and observations (e.g. Stanimirovic et al. 1999).

---

[1] The cooling radius scales as $r_{\mathrm{cool}} \approx 30 n_0^{-0.43}(Z/Z_\odot + 0.01)^{-0.18}$ pc for a supernova explosion with energy $E_{\mathrm{SN}} = 10^{51}$ erg (e.g. Cioffi, McKee & Bertschinger 1988; Thornton et al. 1998; Kim & Ostriker 2015).

Table 2. Summary of our analysed sample of galaxies from THINGS. Column 1: names of galaxy, column 2: distance to galaxy (see Walter et al. 2008), column 3: inclination of galaxy (NB: $0° =$ face-on; see Walter et al. 2008), column 4: H I mass (see Walter et al. 2008), column 5: H$_2$ mass [calculated from column 3, table 5 of Walter et al. (2008) and column 7, table 3 of Leroy et al. (2009)], column 6: stellar mass (see column 8, table 1 of Skibba et al. 2011), column 7: global star formation rate (see column 10, table 1 of Skibba et al. 2011), column 8: H I beam width (calculated from Walter et al. 2008), column 9: simulation of the observed galaxy best matches; viewing perspective; H I mass and stellar mass compared to the MW simulation.

Galaxy	Distance	Inclination	$M_{\mathrm{H\,I}}$	$M_{\mathrm{H_2}}$	$M_\star$	Global SFR	H I beam width	Comments
	(Mpc)	(°)	($10^8\,\mathrm{M_\odot}$)	($10^8\,\mathrm{M_\odot}$)	($10^8\,\mathrm{M_\odot}$)	($\mathrm{M_\odot\,yr^{-1}}$)	(pc)	
NGC 628	7.3	7	38.0	8.3	37.15	1.21	240	LMC-like; face-on; medium H I fraction and low $M_\star$
NGC 3521	10.7	73	80.2	26.5	602.56	3.34	425	MW-like; edge-on; high H I fraction and $M_\star$
NGC 4736	4.7	41	4.0	4.1	218.78	0.43	136	MW-like; face-on; low H I fraction and medium $M_\star$
NGC 5055	10.1	59	91.0	36.2	575.44	2.42	263	MW-like; edge-on; high H I fraction and $M_\star$
NGC 5457	7.4	18	141.7	19.8	107.15	1.49	269	MW-like; face-on; low H I fraction and $M_\star$
NGC 6946	5.9	33	41.5	32.0	91.20	4.76	173	MW-like; face-on; medium H I fraction and low $M_\star$

The gas discs in our simulated galaxies feature a rather elevated oxygen abundance compared with observed values, leading to the average metallicities shown in Table 1. In the case of the MW model, the adopted metallicity is more representative of the inner disc ($R < \mathrm{R_\odot}$) rather than at the solar radius. We have confirmed that this does not affect the conclusions of this paper by re-simulating our LMC-like galaxy with a lower metallicity ($Z = 0.3\,\mathrm{Z_\odot}$).

For the no feedback models (denoted 'noFB'), we adopt a local star formation efficiency per free-fall time of $\epsilon_{\mathrm{ff}} = 1$ per cent. This low efficiency, motivated by the results of e.g. Krumholz & Tan (2007), leads to a galaxy matching the empirical $\Sigma_{\mathrm{SFR}}-\Sigma_{\mathrm{gas}}$ (Kennicutt–Schmidt, KS) relation (Kennicutt 1998; Bigiel et al. 2008), as shown by Agertz et al. (2013), and implicitly assumes regulated star formation, albeit without the explicit action of stellar feedback. In contrast, in the stellar feedback-regulated galaxy models (denoted 'FB'), we adopt a larger efficiency, $\epsilon_{\mathrm{ff}} = 10$ per cent, allowing for feedback to regulate the star formation process back to the observed low efficiencies (e.g. Agertz & Kravtsov 2016), i.e. reproducing the empirical KS relation, while shaping the ISM in the process. These two different models of galaxy evolution (with and without stellar feedback) allow us to investigate the role of feedback in shaping the ISM.

2.3 Observational data

We make use of H I data from THINGS (Walter et al. 2008). The survey focused on galaxies within a distance of 15 Mpc at a resolution of $\sim$6 arcsec, resulting in a spatial resolution (beam size) of $100 \lesssim \ell \lesssim 500$ pc. We select six spiral galaxies from THINGS, all observed close to face-on except for NGC 3521 and NGC 5055.[2] Despite having larger inclination angles, both H I surface density maps of NGC 3521 and NGC 5055 still show clear spiral structure. These six galaxies were selected to give a range in the H I gas mass and similar SFR to our simulated MW-like galaxy. In Table 2, we present the distances, inclination angles, resolution limits, SFRs, and H I, H$_2$ and stellar masses for our sample.

We use the 'robust weighting' data maps from THINGS as these offer higher resolution and a more uniform beam size, see Walter et al. (2008) for a detailed discussion. The zero moment maps are used for calculating properties of the H I density field, such as the two-dimensional density power spectra (see Section 2.4), and the

first moment maps for our analysis of the line-of-sight H I velocity field.

2.4 Computing power spectra

Quantifying the density structure and kinetic energy of the cold ISM using power spectra is common practice in astrophysics, often in the context of turbulent flows, see discussion in Section 1. Throughout this work, we present density and energy power spectrum analysis from both simulations and observations, where we have opted to analyse both sources of data in a similar way as possible to allowing for a direct comparison. As we are working with discrete data, we use the 'Fastest Fourier Transform in the West' (FFTW[3]) routines (Frigo & Johnson 2005) to calculate the discrete Fourier transform. The power spectrum is defined as

$$P(\boldsymbol{k}) = \tilde{\boldsymbol{w}}(\boldsymbol{k}) \cdot \tilde{\boldsymbol{w}}(\boldsymbol{k})^*, \tag{2}$$

where $\tilde{\boldsymbol{w}}(\boldsymbol{k})$ is the Fourier transform of the real array $\boldsymbol{w}(\boldsymbol{x})$ and $\boldsymbol{k}$ is the wavevector. Here '*' refers to the complex conjugate. To obtain an isotropic (one-dimensional) power spectrum, we bin $P(\boldsymbol{k})$ in wavevectors $k = |\boldsymbol{k}|$ and divide each bin by the number of contributing data points (N_k). This gives $\langle P(k)\rangle$ that is commonly referred to as the 'angle-averaged power spectrum' (e.g. Joung & Mac Low 2006). The wavevector $k = 2\pi/\ell$, where ℓ is a physical scale. This allows us to define an *energy spectrum* of the quantify $\boldsymbol{w}(\boldsymbol{x})$ as

$$E(k) \equiv \pi(2k)^{(D-1)}\langle P(k)\rangle, \tag{3}$$

where D is the number of dimensions of the input data.

2.4.1 Surface density power spectra

We quantify the density structure of the observed and simulated ISM by computing the power spectra of H I surface densities following the definition of $\langle P(k)\rangle$ above.

For the observations, we convert the H I data into units of $\mathrm{M_\odot\,pc^{-2}}$ using the 'robust weighted density map' (see Section 2.3) using equation 3 from Walter et al. (2008), combined with the small angle approximation, ignoring inclination effects (we explore the effect of inclination on our results using the simulation data in Section 3.2.4, Fig. 5, Section 3.3.3 and Fig. 9). We use the entire data map, i.e. we do not limit our analysis to a subregion of the maps; therefore, our analysis of observational data takes the entire H I disc into account.

---

[2] For our analysis, we treat *all* THINGS data as face-on galaxies, but explore the role of inclination in our analysis with simulations in Section 3.2.4, Fig. 5, Section 3.3.3 and Fig. 9.

[3] http://www.fftw.org

For the simulations, we calculate surface density maps assuming that the galaxies are 'observed' face-on, i.e. along the axis of rotation, but explore inclination effects in Section 3.2.4, Fig. 5, Section 3.3.3 and Fig. 9. We compute the maps for the simulations at a uniform resolution of $\Delta x = 4.6$ pc, unless otherwise stated. Each map has a size of 36×36 kpc^2, centred on the galaxy centre. The H I map is generated by computing the H I fraction in each cell assuming collisional ionization equilibrium.

To avoid contamination arising from the inherent periodic boundary conditions from the FFT technique, we pad both the simulation and observational data by placing the maps in the centre of a square void domain (zero-padding). The size of the void domain in each dimension is set to 2^n, where n is the first integer where 2^n is greater than the number of cells of the surface density map in the same dimension. Experiments with more padding yielded identical results.

2.4.2 Kinetic energy power spectra

We study the energetics of the ISM by computing 2D kinetic energy power spectra ($E_{\mathrm{KE, 2D}}(k)$) from the simulations and observations, as well as 3D spectra ($E_{\mathrm{KE, 3D}}(k)$) for the simulations. In both the 2D and 3D case, we adopt the definition of the energy spectrum $E(k)$ in equation (3).

For the 3D spectra, we account for compressibility following Kritsuk et al. (2007b), i.e. the variable entering the power spectrum calculations is $\boldsymbol{w} = \rho^{1/2}\boldsymbol{v}$, rather than simply the velocity, where $\boldsymbol{v}$ is the 3D *turbulent* velocity vector in each simulation cell, computed by removing the average galactic rotation at the cell radius, and ρ is the total gas density. We adopt this definition, as this gives us the Fourier transform of the kinetic energy field, but we could instead have used $\boldsymbol{w} = \rho^{1/3}\boldsymbol{v}$, often described as the kinetic energy flux, which has been shown to reproduce energy spectra with Kolmogorov scaling ($E(k) \propto k^{-5/3}$) in supersonic flows (Kritsuk et al. 2007b).

For computational feasibility, we constrain our analysis to a $10 \times 10 \times 5$ kpc^3 region[4] in the plane of the galaxy, centred on the galactic centre. For all energy spectra, we use a uniform resolution of $\sim$9.2 pc, unless otherwise stated. We add padding in each dimension identically to padding added to the surface density maps, then pass the region through FFTW. Due to the non-periodic nature of the disc (in the z-axis),[5] we convolve the input data ($\boldsymbol{w}$) with a Hanning window function[6] before computing the 3D energy spectrum, where the window function extends to $|z| \leq 2$ kpc.

In 2D, relevant for a direct comparison between simulations and observations, we calculate a mass-weighted line-of-sight velocity map[7] for the region described above (i.e. $\boldsymbol{v} \rightarrow v_{\mathrm{los}}$). The velocity map is combined with H I surface density map to give $\boldsymbol{w} = \Sigma_{\mathrm{HI}}^{1/2} v_{\mathrm{los}}$; padding is added in the each dimension of the map before from we calculate $E_{\mathrm{KE, 2D}}(k)$.

For the observed $E_{\mathrm{KE, 2D}}(k)$, we use the first moment (velocity) maps for the THINGS data sets with bulk line-of-sight motion of

the galaxy subtracted. As with the observed H I density maps, we use the entire first moment map when calculating $E_{\mathrm{KE, 2D}}(k)$ for any of our THINGS galaxies.

3 RESULTS

3.1 Overview of simulation results

In Fig. 1, we show edge-on and face-on views of the projected gas density field of the simulated galaxies, with and without stellar feedback, at $t = 350$ Myr. We find clear differences between each of our simulations; the feedback simulations feature galactic winds and fountains, as seen in the edge-on views, and an irregular ISM featuring feedback-driven holes and transient star-forming clouds. The simulations without feedback show little vertical structure as the gas cools down to thin cold discs that fragments into an ensemble of dense rapidly star-forming clouds.

In the left-hand panel of Fig. 2, we show the resulting star formation histories of the simulated galaxies. After an initial transient, all models form stars at a roughly constant rate, where the feedback-regulated galaxies are less efficient in forming stars, despite a local star formation efficiency per free-fall time being 10 times greater ($\epsilon_{\mathrm{ff}} = 10$ per cent versus 1 per cent). In subsequent sections, we carry out all of our analysis at late times ($t > 350$ Myr) when the galaxies have relaxed to a new equilibrium configuration.

Fig. 2 shows that the SMC-like simulations have higher global SFRs than the LMC-like simulations, whereas the opposite is found in observations (see Kennicutt & Hodge 1986; Wilke et al. 2004; Whitney et al. 2008). The origin of this discrepancy is the adopted ICs. The LMC- and SMC-like simulations have comparable total gas masses, but are both $\sim$3 $\times$ more compact than the observed LMC and SMC (see table 1 of Besla et al. 2010). In addition, the SMC's smaller size leads to higher gas densities than in the LMC models, which coupled to a non-linear star formation law ($\dot{\rho}_\star \propto \rho_{\mathrm{gas}}^{1.5}$) results in higher global SFRs.

Our MW-like simulation with feedback features an SFR of $\sim$4 M$_\odot$ yr^{-1} at $t = 450$ Myr, which is a factor of a few greater than observed [Licquia & Newman (2015) found $\sim$1.65 M$_\odot$ yr^{-1} for the MW]. In the LMC-like simulation with feedback, we find an SFR $\sim$0.1$-$0.2 M$_\odot$ yr^{-1} at $t = 450$ Myr, which is a close match to values derived from observations of the LMC, $\sim$0.14 M$_\odot$ yr^{-1} (Murray & Rahman 2010) and $\sim$0.25 M$_\odot$ yr^{-1} (Whitney et al. 2008), thus showing that despite the differences between our simulations and observations, at late times ($t \gtrsim 200$) our MW-like and LMC-like simulations with feedback produce global SFRs that are compatible with those measured from observations.

For our SMC feedback simulation, we find an SFR $\sim$ 0.3–0.4 M$_\odot$ yr^{-1} at $t = 450$ Myr. As noted above, these values are higher than those observed for the real SMC [Wilke et al. (2004) found a value of 0.05 M$_\odot$ yr^{-1}], by a factor of $\sim$8. We remind the reader that we do not aim to recreate an exact match to the real galaxies but instead to produce galaxies with similar gas mass.

With the exception of our LMC-like simulations, our runs without feedback reach similar SFRs to their feedback counterparts by $t = 350$ Myr, i.e. at the beginning of our analysis period. The LMC-like run without feedback has an SFR $\sim$ 4–5 times that of its feedback counterpart.

In the right-hand side of Fig. 2, we show the probability distribution functions (PDFs) for the gas density fields. For an isothermal ISM, numerical and analytical work has shown that the PDF follows a lognormal distribution (e.g. Vazquez-Semadeni 1994; Nordlund & Padoan 1999; Wada & Norman 2001; Wada & Norman 2007),

---

[4] Experiments at lower resolution ($\Delta x \sim 18.3$) with a $10 \times 10 \times 10$ kpc^3 region produce a spectrum with almost identical shape but a slight reduction in power at all scales.

[5] All of the 3D data of interest in the z-axis are contained within the cube.

[6] We use the form $h(z) = 0.5(1 + \cos(2\pi z/H))$, where $h(z)$ is the window function, z is the height above the disc and H is the extent of the function.

[7] Experiments using the line-of-sight velocity dispersion of the gas instead of v_{LOS} yield similar result.
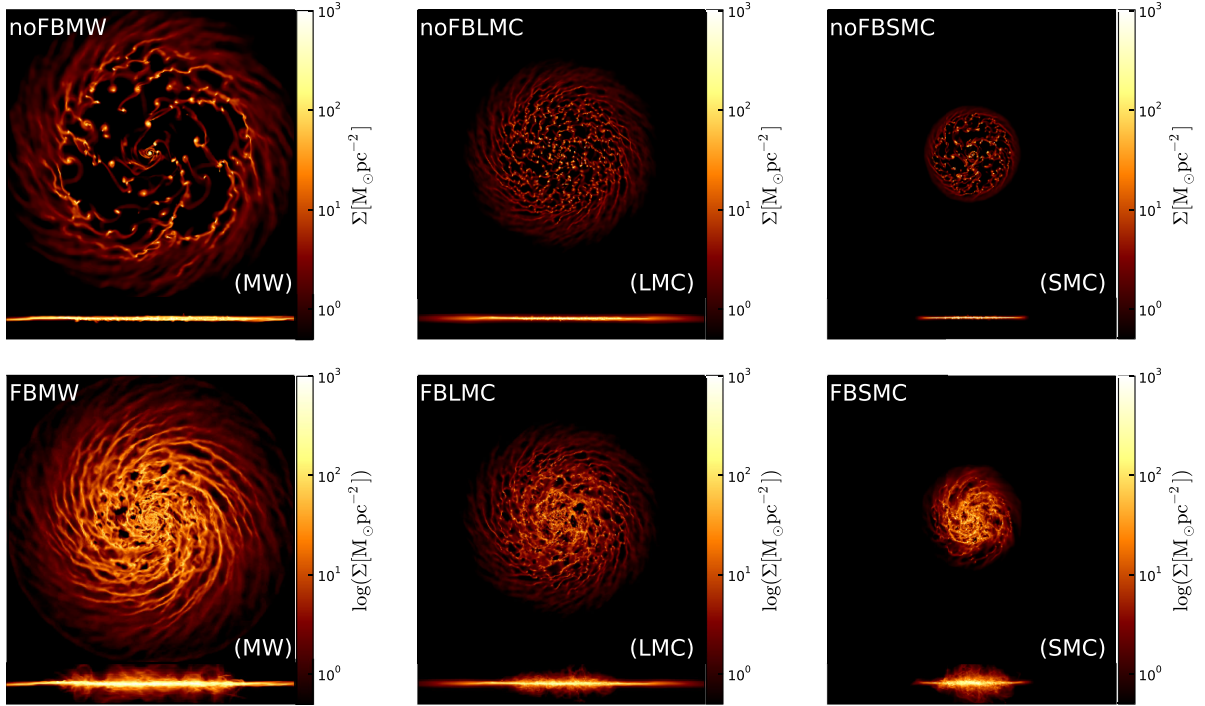
Figure 1. Surface density maps of our simulations at $t = 450$ Myr. The top row shows simulations without feedback while the bottom shows those with feedback. From left to right, we show our MW-, LMC- and SMC-like simulations. Each panel shows the face-on view (36×36 kpc) above the edge-on view (36×5 kpc) for the simulation.
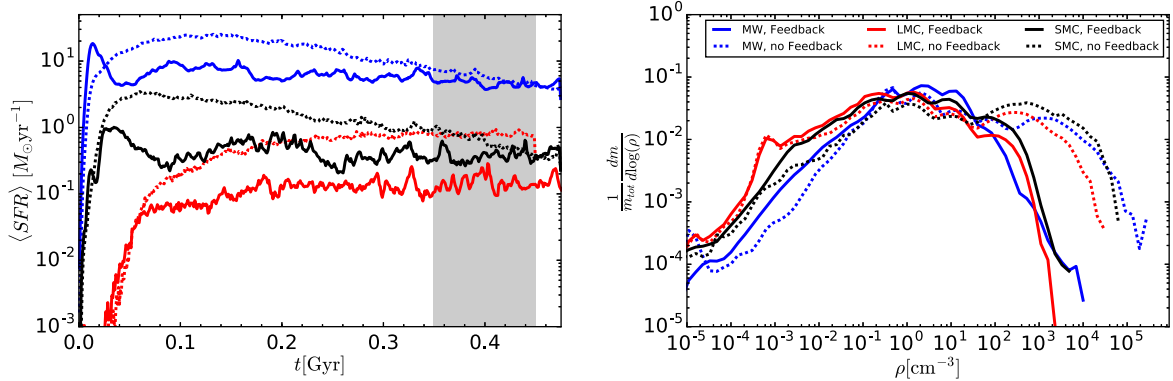

Figure 2. Mean global SFR (left) and PDF (right) for all simulations at $t = 350$ Myr. Feedback runs are shown with solid lines, while no feedback runs are shown with a dashed line. Blue, red and black represent our MW, LMC and SMC simulations, respectively. The shaded region in the left-hand panel shows the period of our analysis, see Section 3.2.2.

or a superposition of multiple lognormal distributions, each corresponding to a separate gas phase (e.g. Robertson & Kravtsov 2008). If self-gravity of the ISM is resolved, then the PDF should develop a power-law tail at high densities (in the MW simulations by Renaud et al. 2013, this occurs for $n \gtrsim 2000$ cm^{-3}).

The effect of stellar feedback is striking; without feedback, gas condenses into dense clouds reaching densities of $n \sim 10^5$ cm^{-3} in all models, albeit slightly lower for the LMC model. Additionally, the PDFs for simulations without feedback do not match lognormal distributions found in previous work of isolated galaxies, but instead resemble the PDFs of galaxies undergoing mergers (see e.g. Renaud et al. 2014). In contrast, in the feedback-regulated simulations, star-forming clouds are dispersed and gas is returned to the ISM in a phase characterized by densities in the range 1 cm$^{-3} \lesssim n \lesssim 10$ cm^{-3}. Gas here reaches maximum

densities around $n \sim 10^3$ cm^{-3}, two orders of magnitude less than in the models neglecting feedback, although most of the dense gas, by mass, reaches only densities of the order of average Giant Molecular Cloud (GMC) densities, i.e. $n \sim$ few 100 cm^{-3}.

In the next sections, we will quantify how feedback affects the ISM as a function of scale and compare this to observations.

3.2 Structure of gas density field

3.2.1 Observations

Fig. 3 shows the surface density power spectra, $\langle P(k) \rangle$, computed as described in Section 2.4.1 with $k = 2\pi/\ell$, for the six galaxies presented in Table 2, together with fitted power-law exponents α, defined by $\langle P(k) \rangle \propto k^{-\alpha}$, as well as the spatial resolution limit. The
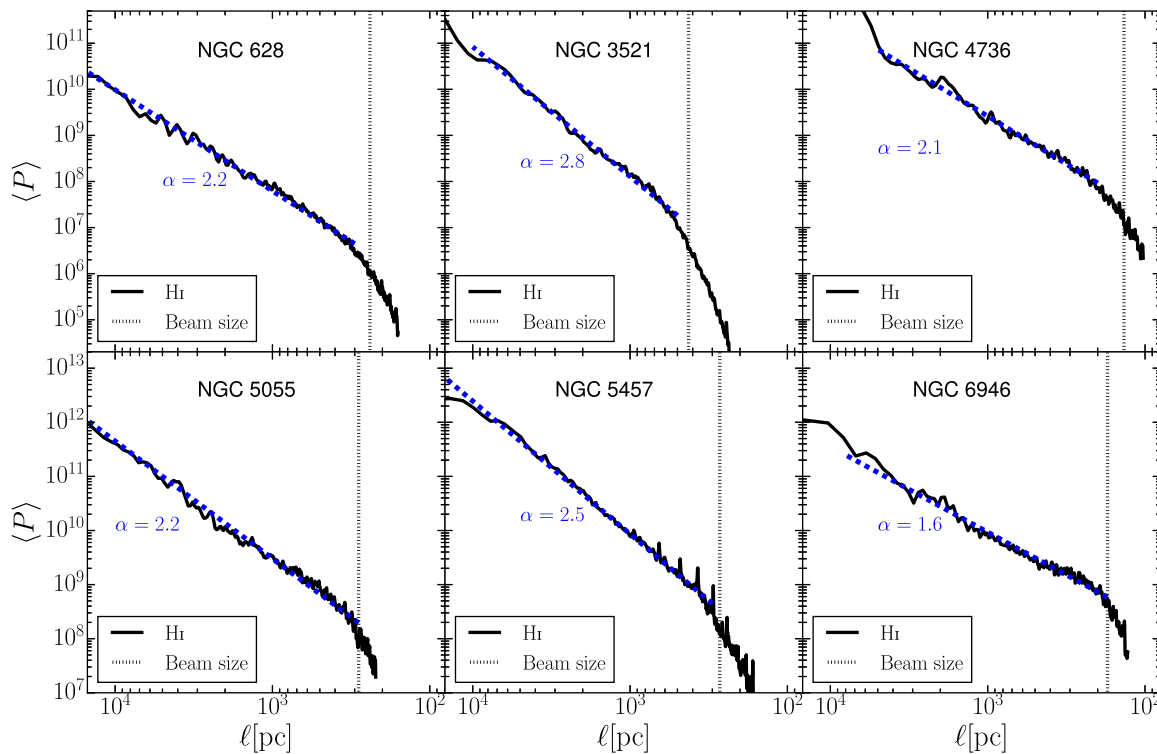
Figure 3. H I surface density power spectra of the six galaxies from the THINGS sample (solid black lines). The beam size is shown by the dotted vertical lines (see Table 2 for values). The blue lines show fitted power laws. The spectra have been normalized (see the text for details).

surface density maps for each galaxy are normalized by the total H I gas mass (M_{HI}) of the galaxy before we calculate power spectra.

We find that the H I power spectra in all galaxies are all well represented by single power laws over a wide spatial range of a few 100 pc up to ∼10 kpc, in agreement with previous studies (e.g. Walker et al. 2014). The power-law exponents are found to be in the range $1.6 \lesssim \alpha \lesssim 2.8$. On scales $\lesssim$ few 100 pc, the spectra steepen, a feature often argued to be an observational signature of the thickness of the gas disc (e.g. Dutta et al. 2009a). Indeed, previous work (e.g. Elmegreen, Kim & Staveley-Smith 2001; Padoan et al. 2001; Dutta et al. 2009a; Zhang et al. 2012) have attributed a break in power spectrum to the scaleheight (h), marking a transition from large-scale 2D turbulence to 3D on scales $\ell \lesssim h$ (but see Combes et al. 2012). However, we find that the breaks in the H I spectra always coincide with the resolution limit of THINGS, making it difficult to make robust claims.

3.2.2 Simulations

In Fig. 4, we show the resulting H I power spectra from the simulated galaxies, computed as described in Section 2.4.1. The solid lines are time-averaged spectra over a period of 100 Myr (separated by $\Delta t = 25$ Myr), starting at $t = 350$ Myr for all simulations, where the shaded regions show the associated 1σ spread in the time-averaged data. We have compared our models presented here to lower resolution simulations ($\Delta x \sim 18.3$ pc) and found that the power spectra steepen on scales $< 10 \Delta x$ (see also Joung & Mac Low 2006). We therefore only present results on scales $> 10 \Delta x$ ($\gtrsim 46$ pc).

The simulated H I spectra differ markedly in the simulations with and without stellar feedback where all three different galaxy mod-

els follow the same trend; $\langle P(k) \rangle$ in models without feedback are more shallow and feature more power on small scales compared to their feedback counterparts, which feature steeper spectra on scales $\lesssim 1$ kpc. The increase in small-scale power in the models without feedback leads to a decrease in $\langle P(k) \rangle$ on large scales ($\gtrsim 1$ kpc), as expected from fragmentation. Interestingly, we find a very small scatter between the analysed simulation snapshots over time, indicating that over an orbital time, the density field is roughly in 'steady state'.

On scales $\ell \lesssim 1$ kpc, the power-law fits to the LMC simulation are in good agreement with observations (Elmegreen et al. 2001; Block et al. 2010). Indeed, Block et al. (2010) found that power spectra of LMC emission at 24, 70 and 160 μm have a two-component power-law structure with a shallow slope of 1.6 for $\ell \gtrsim 100$ pc, and a steep slope of 2.9 on smaller scales, in excellent agreement with our LMC simulation including feedback, but in stark contrast to the model without.

Stanimirovic et al. (1999) calculated an $\alpha = 2.85$ for the SMC, while Pilkington et al. (2011) found $\alpha = 3.2$, on all scales $\ell < 7$ kpc. Such steep spectra are not recovered in our models, except for $\ell < 100$ pc. Our SMC model with feedback is quite well fitted by a single power law on scales $100 < \ell < 7$ kpc, in agreement with observations, but with a shallower slope. It is possible that the differences here arise due to the definition of $\langle P(k) \rangle$, e.g. being angle-averaged or not, which we leave for a future investigation. Furthermore, the lack of a cosmological environment may affect our results, as the LMC and SMC are passing through the MW halo and experience strong tidal forces. Such forces produce large-scale structures such as the Magellanic Bridge and Magellanic Stream, which would increase the power on large scales.

Finally, we note that all measured H I spectra steepen on small scales, with a break around $\ell_{break} \sim 100 - 200$ pc for all simulated
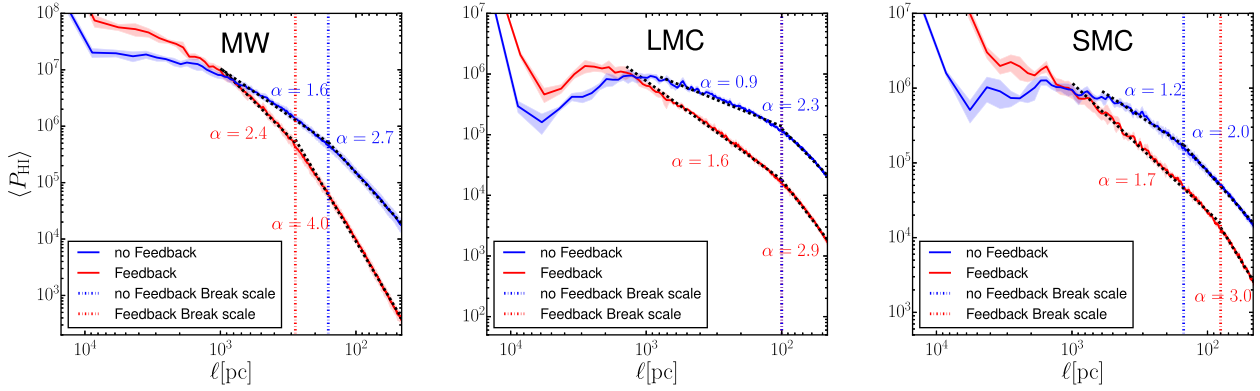
Figure 4. Time-averaged surface density power spectra using H I gas for our simulations. From left to right, we show the resulting spectra from the MW, LMC and SMC models with feedback shown in red and no feedback shown in blue. The dashed black lines show our power-law fits with gradients next to each fit. The red and blue vertical dot–dashed lines indicate the position of the break in the power law. The shaded regions around each power spectrum show the 1σ deviation from the mean.
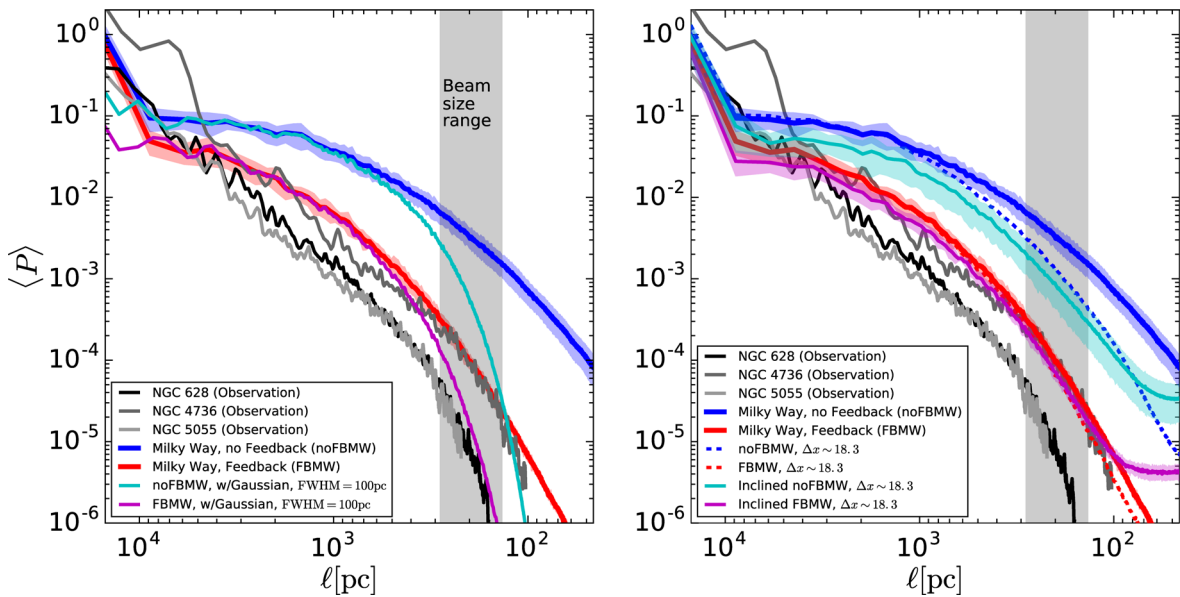

Figure 5. Direct comparison of H I surface density power spectra of NGC 628, 4736 and 5055 (black, dark grey and grey solid lines, respectively) from our THINGS sample and our MW simulation (red and blue solid lines). The grey shaded region indicates the range of beam sizes given for the subset of THINGS. Left-hand panel: we show the effect of first convolving the surface density map of the feedback (magenta) and no feedback (cyan) runs with a Gaussian (FWHM = 100 pc). Right-hand panel: time-averaged power spectra of the simulations when analysed at $\Delta x \sim 18.3$ pc (dashed lines) and $\Delta x \sim 4.6$ pc (solid lines). Overplotted are the time-averaged spectra of the simulations inclined at $40°$, with feedback (magenta) and without feedback (cyan) at a resolution of $\Delta x \sim 18.3$ pc.

galaxies featuring feedback. This scale is resolved in all models, and coincides with the thickness of the H I layer, in agreement with the analysis of Dutta et al. (2009a), as discussed above.

3.2.3 Direct comparison

In the left-hand panel of Fig. 5, we compare $\langle P(k) \rangle$ from the simulated MW-like galaxy directly to a subset of the THINGS sample (NGC 628, 4736 and 5055). This subset was selected to compare a range of masses and inclination angles to our simulated galaxies. To compare the relative power and shape of the spectra, we normalize the surface density map of each galaxy (simulation and observation) by the H I mass within 1 half-light radius ($r_{1/2}$) from the galactic centre. For NGC 628, 4736 and 5055, this corresponds to $r_{1/2} = 5$, 1.75 and 4.7 kpc, respectively (values from Belley &

Roy 1992; Thornley 1996; Martin & Belley 1997) while for our MW simulations this corresponds $r_{1/2} = 3.1$–3.2 kpc, depending on the snapshot.

The feedback model is in good agreement with observations in terms of relative power on all scales, and is an especially good match to NGC 4736, which like our simulations is more compact than NGC 628 or 5055, and features a factor of a few less power on scales $\ell \lesssim 5$ kpc. The fact that stellar feedback can affect the distribution of H I up the several kpc, rather than typical scales of SN bubbles (<100 pc), is dramatic and illustrates its importance for galaxy evolution.

As discussed above, $\langle P(k) \rangle$ from observations are better fitted by a single power law compared to the simulations. This is not necessarily due to the effect of stellar feedback, but rather the presence of a more extended H I disc that is not present in our ICs. Indeed, extended low-density H I discs and structures are observed out to large
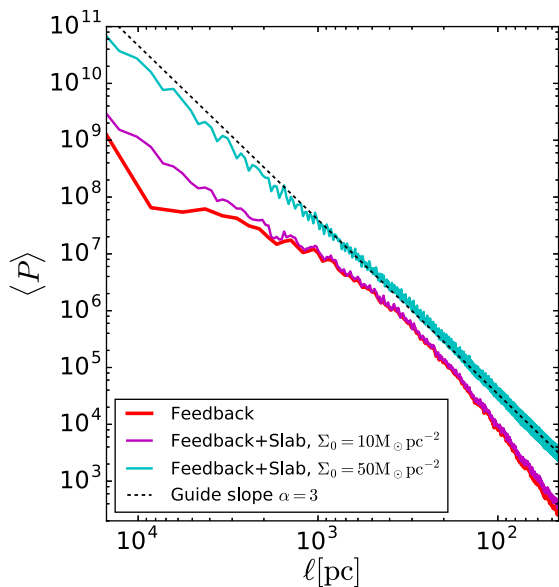
Figure 6. Summary of slab experiments. We show the power spectra of our MW feedback simulation at $t = 400$ Myr with the addition of a uniform slab, which is added to the data before calculating the power spectrum. Shown are two slabs with different surface densities $\Sigma_0 = 10$ M$_\odot$ pc^{-2} (magenta line), $\Sigma_0 = 50$ M$_\odot$ pc^{-2} (cyan line) and the simulation without slab (red line). The dashed (black) line shows a power-law slope of $\alpha = 3$. The spectra are all normalized via their half-light radius (see Section 3.2.3).

galactic radii ($R \sim 100$ kpc; Oosterloo et al. 2007; Scott et al. 2014). Bigiel et al. (2008) found extended H I distributions around several of the THINGS spirals and dwarf irregulars at a nearly constant $\Sigma \sim 10$ M$_\odot$ pc^{-2} out to at least one optical radius (r_{25}). A more extreme example is the compact dwarf galaxy NGC 2915 that is surrounded by a very extended H I disc ($r \gg r_{25}$), unable to forms stars (Meurer 1994; Meurer et al. 1996). The source of these extended regions is still not clear, but is currently thought to be a remnant of cosmological accretion or the result of mergers and interactions between galaxies (Oosterloo et al. 2007, and reference within). Our simulations use an exponential surface density profile for the ICs, which more closely resembles the observed stellar and H$_2$ distributions. To investigate whether the lack of large-scale H I in our simulations can be the cause of the difference between observations and simulation at large scales, we add a low surface density extended distribution of gas to our simulated galaxies before calculating the power spectra.

In Fig. 6, we show the results for a uniform density distribution of gas ($\Sigma(r) = \Sigma_0$) being added to all cells, with $\Sigma_0 = 10$ or 50 M$_\odot$ pc^{-2}. In both cases, the added gas boosts the power on large scales, leading to a steepening of the spectra. In the case of $\Sigma_0 = 50$ M$_\odot$ pc^{-2}, $\langle P(k) \rangle$ becomes relatively well fitted by a single power law, in good agreement with observations, albeit with a larger power-law exponent than observed ($\alpha \sim 3$). We note that the analytical expectation[8] for the power spectrum of a uniform disc is indeed $P(k) \propto k^{-3}$. In the case of more complex structure, such as galaxies, the power spectrum is a superposition of the uniform disc plus the signal from the 'fine' structure of the galaxy, i.e. GMCs

and spiral arms. $\Sigma \geq 50$ M$_\odot$ pc^{-2} is an unusually high H I surface density at large galactic radii (Bigiel et al. 2008), and should be considered an extreme case, but illustrates that missing extended gas will affect the shape of $\langle P(k) \rangle$.

Finally, both observational and simulated data contain smearing of the signal on the smallest scales due to limited resolution, which could affect analysis of such data. We briefly explore this effect on the observed density power spectra by convolving the surface density maps of our MW simulations with a Gaussian prior to calculating the power spectra. Fig. 5 shows the results for a Gaussian with a full width at half-maximum (FWHM) equal to 100 pc on $\langle P(k) \rangle$.[9] We find that this procedure removes power on scales less than $\sim 3 - 4 \times$ of the FWHM, hence affecting the overall shapes of the spectra. This effect can be dramatic, but does not lead to difficulties in disentangling the effect of stellar feedback (when the spectra are appropriately weighted). In our models, the overall match to observations in the absence of feedback is always poor, regardless of choice of smoothing scale, indicating that this effect is subdominant for the THINGS sample.

3.2.4 Effect of inclination

In the previous sections, we considered all observed galaxies as face-on, i.e. $i = 0°$. However, as shown in Table 2, this is not the case for our THINGS sample. We explore the effect of inclination of the galaxy on the power spectrum by observing our simulated galaxies at an $i = 40°$ inclination, which is the mean inclination in our THINGS sample. For computational feasibility, we analyse the simulation at a resolution of $\Delta x \sim 18.3$ pc for both the density power spectra and the 2D kinetic energy spectra. We note that reducing the resolution of the analysis has the effect of removing small-scale power from the no feedback simulations, but very little effect on the feedback runs.

The right-hand panel of Fig. 5 shows the effect of inclining the galaxy on the surface density power spectrum, compared to the face-on case only a small increase in power on scales of small scales ($\ell \lesssim 100$ pc) in both feedback and no feedback runs. This is expected due to the increase in column density introduced by inclining the galaxy, but on larger scales we find very little change in the shape of the spectra in both cases. From these results, we conclude that the effect of inclination on a density power spectrum is to increase power on small scales, and leave large scale unaffected, making it possible to 'observe' the effect of feedback directly without inclination correcting.

3.3 Kinetic energy of the ISM

In this section, we analyse the impact of feedback on the velocity structure of the simulated and observed ISM. As described in Section 2.4.2, we do so by computing the 2D line-of-sight kinetic energy power spectrum ($E_{\rm KE, 2D}(k)$) for the simulated and observed galaxies, as well as full 3D spectra ($E_{\rm KE, 3D}(k)$) for the simulations, allowing us to compare the results to well-known expectations of turbulent scalings for incompressible Kolmogorov turbulence ($E(k) \propto k^{-5/3}$) and compressible supersonic turbulence ($E(k) \propto k^{-2}$).

---

[8] The Fourier transform ($\tilde{f}(k)$) of uniform disc is given by $\tilde{f}(k) \propto \frac{J_1(ak)}{k}$, where J_1 is the Bessel function of the first kind of order 1. In the regime of this work $ak \gg 1$ and therefore $J_1 \sim (ak)^{-1/2}$. $\tilde{f}(k)$ then becomes proportional to $k^{(-3/2)}$ making the power spectrum proportional to k^{-3}.

[9] We follow the standard definition of a Gaussian, $\phi(x) = a e^{-(x-b)^2/(2c^2)}$, where a is normalizing constant, b is the position of the peak of the Gaussian and $c = {\rm FWHM}/(2\sqrt{2 \ln 2})$.
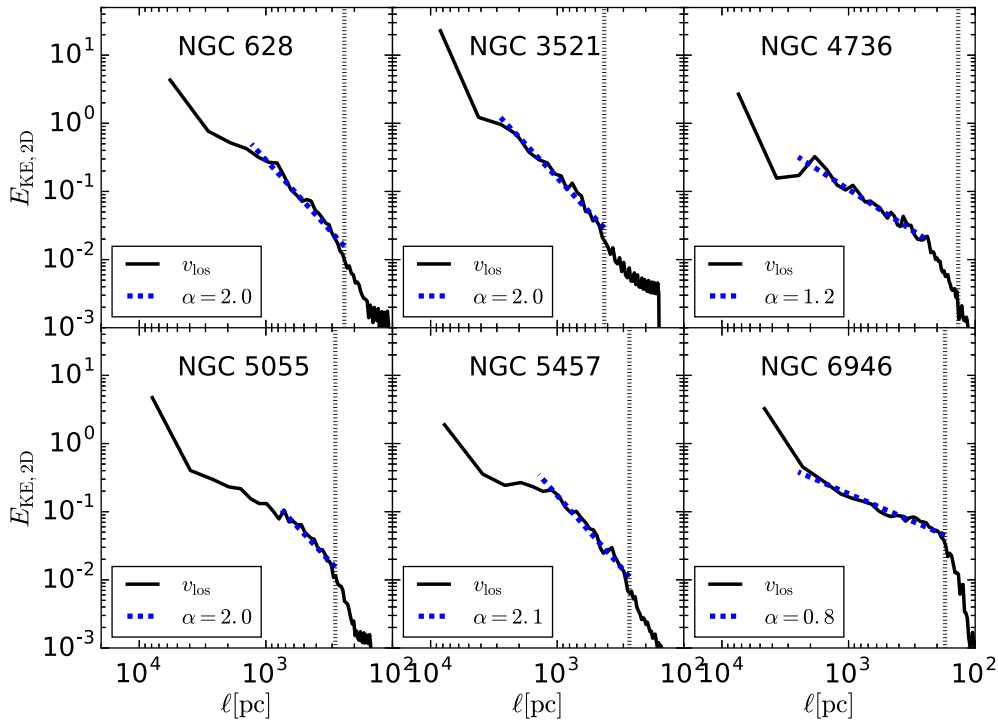
Figure 7. 2D kinetic energy ($\Sigma_{\rm HI}^{1/2} v_{\rm los}$) power spectra for our THINGS sample (black solid lines). The blue dashed line shows a fitted power law to the spectra, with the gradient of the slope given in legends. The vertical black dotted line shows the beam width for each galaxy (see Table 2 for values). The $E(k)$ presented here have all been normalized (see Section 3.3.3 for details).

3.3.1 *Observations*

In Fig. 7, we show the line-of-sight $E(k)$ from the THINGS galaxies. Four of the galaxies in our sample (NGC 628, 5055, 5457 and 3521) feature steep power spectra on scales above the resolution limit, with $E(k) \propto k^{-\alpha}$ and $\alpha \sim 2$, suggesting that the ISM of these galaxies is compressible and supersonic. All but the latter galaxy feature a reduction in steepness in the spectra on scales $0.5\,{\rm kpc} \lesssim \ell \lesssim 1\,{\rm kpc}$, possibly related to disc thickness.

The ISM in the starburst galaxy NGC 4736 is rather different compared to the other galaxies, with a large ring of cold gas and young stars in its central region. This is possibly the origin of the more shallow $E(k)$ measure in this galaxy on $\sim {\rm kpc}$ scales, with $\alpha \sim 1.2$, indicating that the contribution from small scales is significant. NGC 6946 features an even shallower $E(k)$, with $\alpha \sim 0.8$. This galaxy also has a complicated dynamical structure, with three nested bars, a double molecular disc and a nuclear starburst region (Romeo & Fathi 2015). The velocity map of NGC 6946 (see fig. 65, bottom-left panel of Walter et al. 2008) shows large structures, with sizes of $\sim 5\,{\rm kpc}$ or greater, with little variation ($\Delta v \lesssim 25\,{\rm km\,s^{-1}}$) in velocity. These relatively uniform regions could possibly account for the shallower shape of $E_{\rm KE,\,2D}(k)$.

3.3.2 *Simulations*

In Fig. 8, we show $E_{\rm KE,\,2D}(k)$ for all simulations, using only the line-of-sight velocity field as observed face-on. As for the density spectra, we show the time-averaged spectra of the feedback/no feedback simulations for the MW, LMC and SMC simulations, respectively, and we only show result down to 10 resolution elements ($10\Delta x$).

We again find a dramatic difference between the feedback and no feedback simulations; feedback regulation results in steep power

spectra, with $\alpha \sim 2\text{--}3$ on scales $\lesssim 0.5\,{\rm kpc}$, with a transition into shallower relations on large scales, in good agreement with the subset of the observations discussed above. Most power in the feedback run is hence present on large ($\,{\rm kpc}$) scales, with a cascade to small scales. Without feedback, $E_{\rm KE,\,2D}(k)$ *increases* down to scales of a few $100\,{\rm pc}$ for all simulated galaxies, indicating the presence of dense cloud structures, and turns over on smaller scales. Large-scale turbulence imparted by large-scale rotation and gravitational instabilities is no longer present, as power has cascaded once into dense star-forming clouds where it is 'locked up' instead of being disrupted and returned to the large-scale driving. We will explore these concepts more in future work (Agertz et al., in preparation).

3.3.3 *Direct comparison*

In Fig. 9, we directly compare[10] $E_{\rm KE,\,2D}(k)$ from the MW-like simulations to a subset of THINGS sample (NGC 628, 4736 and 5055). Without feedback, we find an excess of power on small scales ($\ell \lesssim 200\text{--}300\,{\rm pc}$), and a significant lack of power on large scale with a peak in the spectrum on intermediate scales. However, the feedback runs provide a better match to observations on all scales. This highlights the role of stellar feedback, together with gravity and shear, in regulating the energetics of the ISM on all scales. $E_{\rm KE,\,2D}(k)$ from the feedback-regulated simulations are a better match to observations for $\ell < 1\,{\rm kpc}$, indicating that our adopted feedback model can readily predict the scale dependence of the (line-of-sight) kinetic energy field of real galaxies on small scales.

---

[10] To enable this direct comparison, we normalize $E_{\rm KE,\,2D}(k)$ by enforcing $\int_{\ell=0.1\,{\rm kpc}}^{\ell=1\,{\rm kpc}} E(k){\rm d}k = 1$.
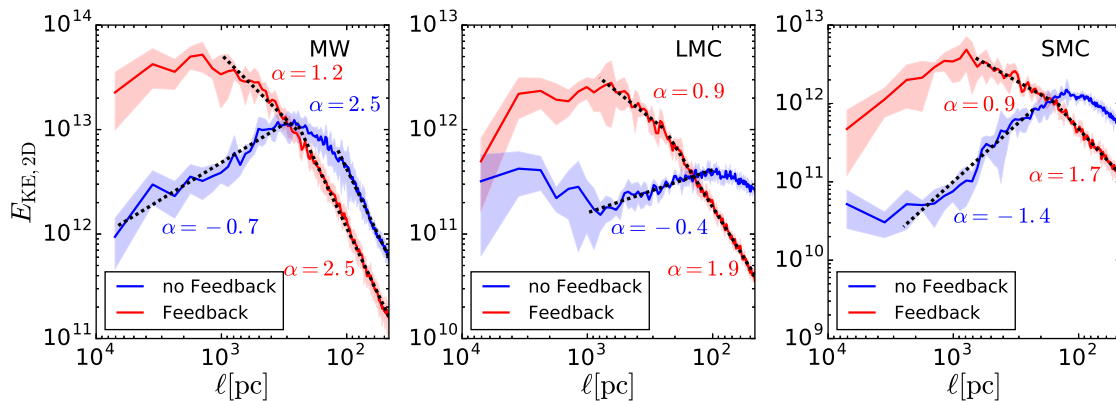
Figure 8. 2D kinetic energy ($\Sigma_{\mathrm{H\,I}}^{1/2} v_{\mathrm{los}}$) time-averaged power spectra for our simulations. From left to right, we show the resulting spectra from the MW, LMC and SMC models with feedback shown in red and no feedback shown in blue. The dashed black lines show our fitted power law with gradients next to each fit. The shaded regions around each power spectrum show the 1σ deviation from the mean. The $E(k)$ presented here have *not* been normalized.
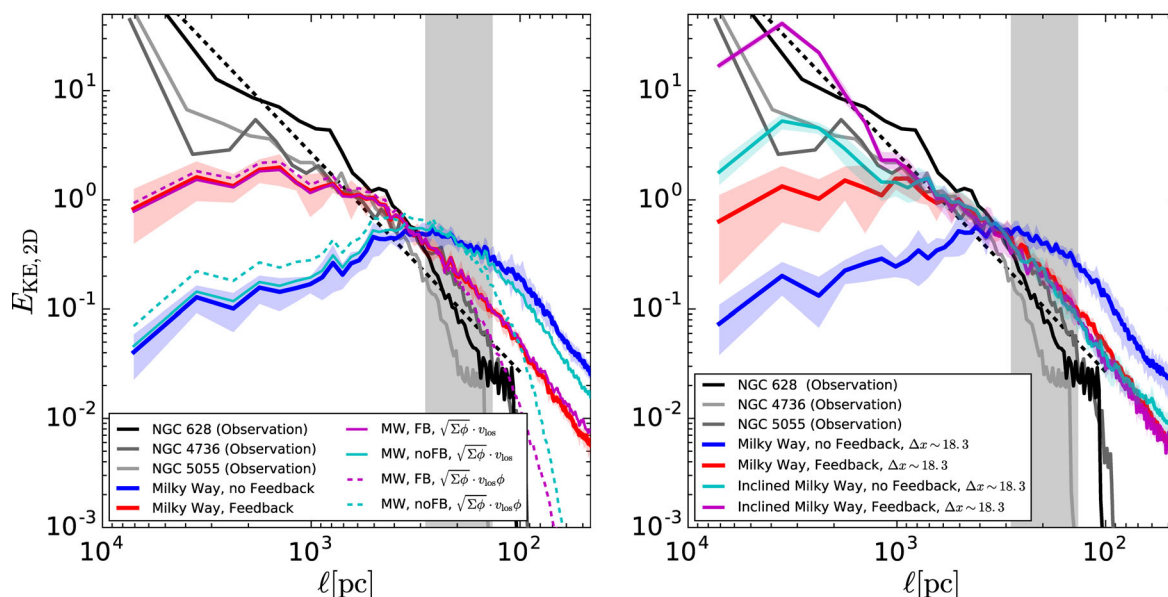

Figure 9. Direct comparison of the 2D kinetic energy ($\Sigma_{\mathrm{H\,I}}^{1/2} v_{\mathrm{los}}$) power spectra of NGC 628, 4736 and 5055 (black, dark grey and grey solid lines, respectively) from our THINGS sample and our MW simulation (red and blue solid lines). The grey shaded region indicates the range of beam sizes given for the subset of THINGS. Left: shown in magenta (feedback) and cyan (no feedback) are the results of first convolving the surface density map (solid lines) and the surface density map as well as the velocity map (dashed lines) with a Gaussian (FWHM = 100 pc). Right: inclination test. Time-averaged spectra of the simulations inclined at $40°$ are shown in magenta (feedback) and cyan (no feedback). All simulation spectra in this panel are calculated at a resolution of $\Delta x \sim 18.3$ pc. These spectra are all normalized, see Section 3.3.2 for details.

An even closer agreement on sub-kpc scales is found when smoothing the simulated data, as show in Fig. 9. Smoothing,[11] again using a Gaussian with a FWHM = 100 pc, predominantly gives rise to less small-scale power that brings the feedback model to overlap with observations. The model without feedback is affected in a similar way, but is still inconsistent with the observations on all scales.

What about the observed large-scale power? The right-hand panel of Fig. 9 shows the effect of inclination of $E_{\mathrm{KE,\,2D}}(k)$, carried out in the same manner as in Section 3.2.4. When inclined we find that

the non-turbulent rotational velocity dominates the entire signal, which brings both the feedback and no feedback model into close agreement with observations. For line-of-sight energy spectra to be able to differentiate feedback models, careful subtraction of the gas rotational velocity is needed, e.g. using 'tilted-ring model' (Rogstad, Lockhart & Wright 1974) or 3D analogues such as the method of Teodoro & Fraternali (2015), as used to model H I rotation curves of dwarf galaxies (Read et al. 2016b,c). Such an analysis is beyond the scope of this work.

3.4 3D energy spectra

We now turn to the full 3D kinetic energy $E(k)$ (see Section 2.4.2), which we show in Fig. 10 for all three galaxy sizes. As for the

---

[11] We explore two regimes of smoothing: applying a Gaussian (ϕ) only to the surface density map ($\sqrt{\Sigma_{\mathrm{H\,I}}\phi} \cdot v_{\mathrm{los}}$) and applying the Gaussian to both the surface density map and line-of-sight velocity map ($\sqrt{\rho\phi} \cdot v_{\mathrm{los}}\phi$).

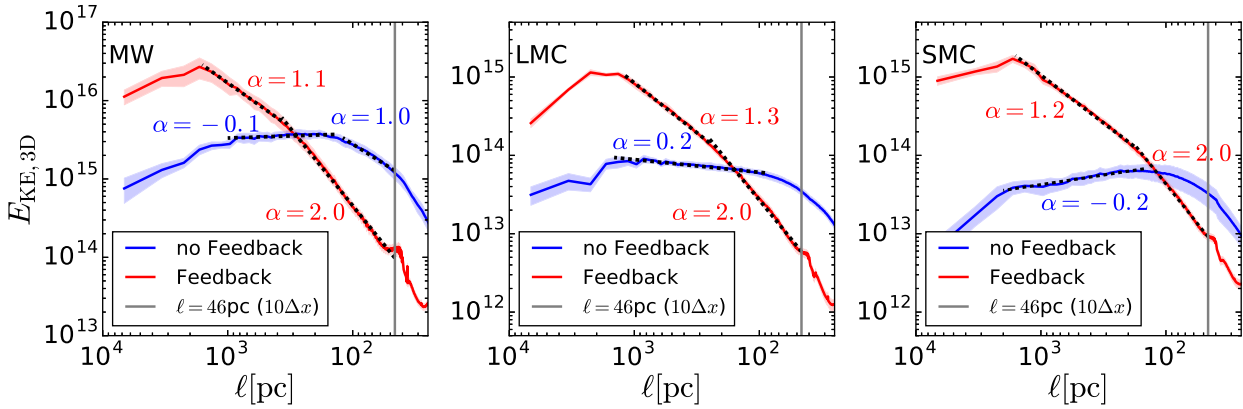**Figure 10.** Full 3D kinetic energy ($\rho_{\mathrm{all}}^{1/2}\boldsymbol{v}$) power spectra for each galaxy (MW – left, LMC – centre and SMC – right) using the full 3D velocity field ($\boldsymbol{v}$). Each panel shows the time-averaged spectra (solid colour lines) and the 1σ deviation from the time average (shaded colour region). The black (dashed) lines represent various gradients that are detailed in the panel. Red represents feedback simulations and blue no feedback simulations in all panels. The minimum trusted scales are shown with the vertical black line.

2D case, the feedback simulations feature a much steeper power spectrum compared to their no feedback counterparts. Without feedback power cascades to, and remains, on small scales, hence creating shallow energy spectrum with a steepening occurring on scales of individual clouds. In all three galaxy models, feedback maintains power-law slopes of almost exactly $\alpha = 2$ on scales $\lesssim$ several 100 pc, as expected in supersonically turbulent flows. On scales $\gtrsim$ few 100 pc, a more shallow scaling of $E_{\mathrm{KE,\,3D}}(k)$ is measured, possibly indicating the thickness of the simulated discs. The spectra feature very little scatter over time, indicating that turbulence driven by stellar feedback and, coupled with the large-scale driving, has reached steady state over the time-scale that we carry out analysis.

These results complement previous results in the literature. For example, Joung & Mac Low (2006), Martizzi et al. (2016) and Padoan et al. (2016) modelled SN-driven turbulence in isolated small-scale boxes (<1 kpc) and measured $E(k)$, finding that power on small scales ($\ell \lesssim 100$ pc) follows $E(k) \propto k^{-2}$. On larger scales, their energy spectra become shallower and feature significantly less power than what we predict here, illustrating that full galactic models are necessary to account for the transfer of energy between scales inside of galaxies. In future work, we will explore the driving scale of the $E(k)$ and the interaction between small-scale driving (stellar feedback) and large-scale driving (gravity).

We have also performed the same analysis on the three velocity components in a cylindrical coordinate system (v_z, v_r and v_θ) for the simulated MW galaxy, and find close to identical scalings for each component as for the total kinetic energy field in the feedback simulation, see Fig. 11, with the radial component containing most of the power. In the no feedback case, we see a significant difference between the three components, with $E_{v_z} < E_{v_\theta} < E_{v_r}$ on all scales. The lack of feedback here leads to little power in the vertical component, being ~2 dex lower compared to its feedback counterpart.

Bournaud et al. (2010) found, using high-resolution models of an LMC-like galaxy, that $E(k)$ of v_r and v_θ are almost identical, while v_z follows shallower power law up to scales of $\ell \sim 200-300$ pc before levelling off. The reason for this discrepancy could be due to the nature of their feedback model, e.g. the lack of pre-SN feedback limits the effectiveness of the SNe for not just the density power spectra (see Section 4.1) but also for $E(k)$.
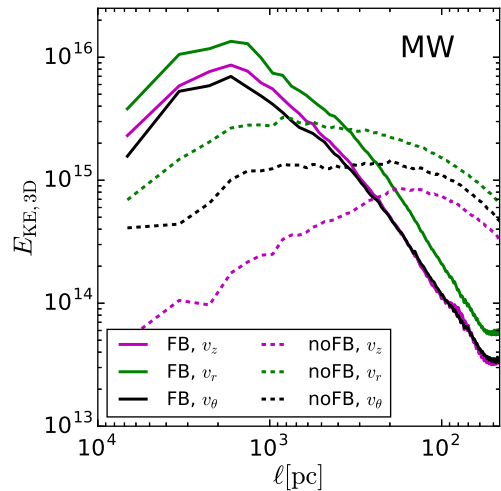

Figure 11. Time-averaged 3D kinetic energy ($\rho_{\mathrm{all}}^{1/2}\boldsymbol{v}_c$) power spectra for each velocity component of the MW simulations. We show the vertical (v_z, magenta), radial (v_r, green) and tangential (v_θ, black) velocity components. We distinguish between feedback and no feedback with solid and dashed lines, respectively. We note that we have not normalized, i.e. they show the relative power of each component.

3.5 Velocity or density fluctuations?

It is unclear from the above analysis what gives rise to the measured energy spectra. It is possible that $E(k)$ for our simulations is driven by fluctuations in the density field only, i.e. $E(k)$, as defined here, is just a measure of $\sqrt{\Sigma_{\mathrm{H\,I}}}$ (2D) or $\sqrt{\rho_{\mathrm{all}}}$ (3D), with random fluctuations from the velocity component superimposed on to the spectra. To test this possibility, we compare the spectra of $\Sigma_{\mathrm{H\,I}}^{1/2}v_{\mathrm{los}}$, v_{los} and $\Sigma_{\mathrm{H\,I}}^{1/2}$ in 2D and $\rho_{\mathrm{all}}^{1/2}\boldsymbol{v}$, $\boldsymbol{v}$ and $\rho_{\mathrm{all}}^{1/2}$ in 3D for our MW-like simulation in Fig. 12. Henceforth, we refer to these quantities as $E_{\mathrm{KE,\,2D}}(k)$, $E_{v_{\mathrm{los}}}(k)$, $E_\Sigma(k)$, $E_{\mathrm{KE,\,3D}}(k)$, $E_{\boldsymbol{v}}(k)$ and $E_\rho(k)$, respectively. Note that in order to facilitate a comparison of the shape of the spectra, we normalize them to the same power at $\ell = 46$ pc.

For the feedback model, we find that $E_{\mathrm{KE,\,2D}}(k)$ and $E_{v_{\mathrm{los}}}(k)$ are very similar, indicating that the energy spectrum is shaped by the velocity fluctuations. In the 3D feedback case, we find that on scales less than a few 100 pc, $E_{\mathrm{KE,\,3D}}(k)$ and $E_{\boldsymbol{v}}(k)$ trace each other, although $E_{\boldsymbol{v}}(k)$ features a lot of noise, while on large scales $E_{\boldsymbol{v}}(k)$
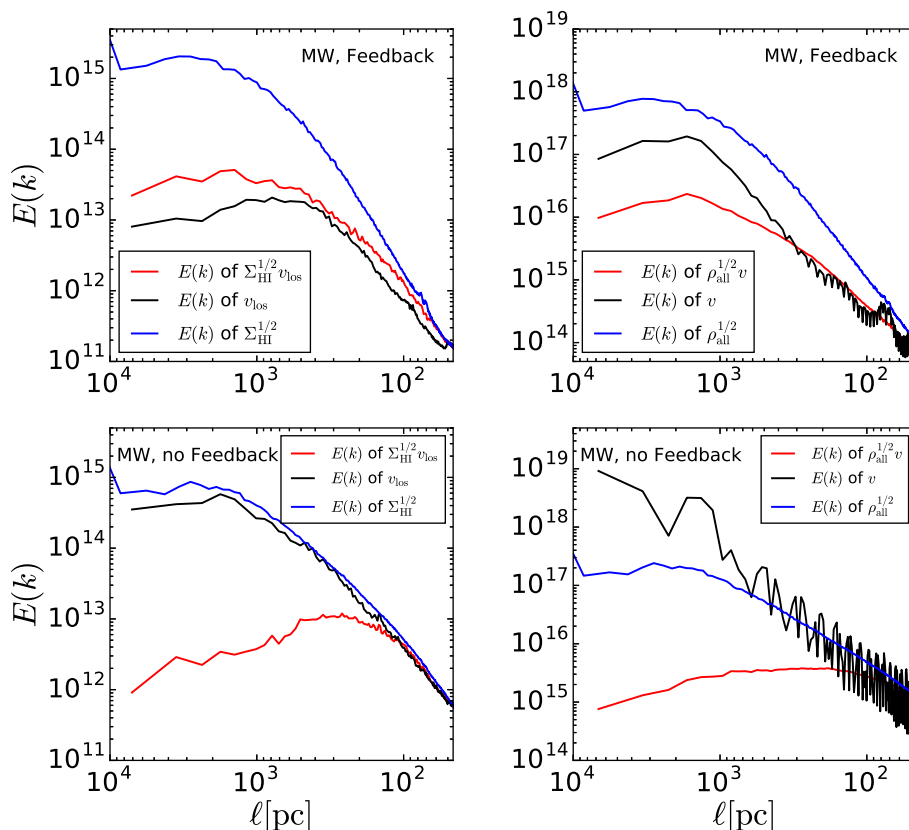
Figure 12. Comparison of the spectra for $\Sigma_{\mathrm{H\,I}}^{1/2} v_{\mathrm{los}}$, v_{los} and $\Sigma_{\mathrm{H\,I}}^{1/2}$ (left-hand panels) and $\rho_{\mathrm{all}}^{1/2} \boldsymbol{v}$, $\boldsymbol{v}$ and $\rho_{\mathrm{all}}^{1/2}$ (right-hand panels). Top: comparison of simulation including feedback. Bottom: comparison of simulations neglecting feedback. The spectra are normalized to the value of $E(k)$ for $\Sigma_{\mathrm{H\,I}}^{1/2} v_{\mathrm{los}}$ (left-hand panels) and for $\rho_{\mathrm{all}}^{1/2} \boldsymbol{v}$ (right-hand panels) at $\ell = 46\,\mathrm{pc}$.

increases in power. This *relative* increase in power may be due to feedback-driven outflows of tenuous gas venting out of the disc (see the edge-on view in the bottom left of Fig. 1). Both $E_\Sigma(k)$ and $E_\rho(k)$ poorly match the respective velocity and kinetic energy spectra, suggesting that the velocity fluctuations play an important role in explaining the kinetic energy spectrum when feedback is present.

Without stellar feedback, $E_{v_{\mathrm{los}}}(k)$ and $E_\Sigma(k)$ are almost identical, i.e. the velocity structure of the gas appears to trace that of the density. However, combining these two produces a non-linear result, here a turnover at $\ell \sim 200-300\,\mathrm{pc}$, with little power present on large scales. $E_v(k)$ and $E_\rho(k)$ show a similar behaviour for $\ell \lesssim 1\,\mathrm{kpc}$, with significant noise[12] in the velocity component, before diverging at larger ℓ.

From these comparisons, we conclude that the kinetic energy spectra we present for $\Sigma_{\mathrm{H\,I}}^{1/2} v_{\mathrm{los}}$ and $\rho_{\mathrm{all}}^{1/2} \boldsymbol{v}$ are not driven by the density field alone.

3.6 Compressive versus solenoidal motions

Having established that energy spectra of the turbulent gas in galaxies with and without stellar feedback differ markedly on all scales, it is interesting to explore how stellar feedback affects the nature of turbulence by computing the fraction of kinetic energy present in compressive[13] (curl-free, $\nabla \times \boldsymbol{v} = \boldsymbol{0}$) and solenoidal[14] (divergence-free, $\nabla \cdot \boldsymbol{v} = 0$) motions. This is an important characteristic of the ISM, e.g. the shape of the density PDF depends on the type of turbulent forcing, as demonstrated by numerical simulations of supersonic flows (e.g. Padoan, Nordlund & Jones 1997; Federrath et al. 2010; Federrath & Klessen 2013).

In compression-dominated turbulence, regions with an excess of dense gas widen the PDF from the expected case of isothermal supersonic turbulence of non-self-gravitating gas (Vazquez-Semadeni 1994; Nordlund & Padoan 1999; Wada & Norman 2001). This in turn shifts the median of the PDF to larger densities. For an ISM that has reached equipartition, it is expected that 2/3 of the kinetic energy is in solenoidal motions and 1/3 in compressive (Padoan et al. 1997; Kritsuk et al. 2007a; Federrath et al. 2010; Renaud et al. 2013, 2014, and references within). The ratio of 2:1 is determined by the dimensionality of each mode, i.e. compression only has one degree of freedom, while solenoidal modes have two.

Renaud et al. (2014) noted that compression-dominated turbulence is induced by tides during galaxy interactions, and triggers the observed starburst activity over kpc-scale volumes. However, the role of compressive turbulence appears to be less important in more quiescent environments like isolated disc galaxies, where turbulence remains close to equipartition (i.e. solenoidal-dominated

---

[12] This behaviour likely originates from sharp features in the velocity field, leading to oscillations in the Fourier-transformed quantities (this is the familiar 'Gibbs' phenomenon; Riley, Hobson & Bence 2006).

[13] Compressive modes include both compression and rarefaction of the gas.
[14] Some authors refer to solenoidal modes as vorticity.

regime; Renaud et al. 2015). There, the Mach number is the main driver of gas overdensities, and thus star formation.

To better understand the nature of the ISM turbulence in our simulations, we calculate the fraction of energy in each component via

$$f_m = \sum_{i=1}^{n} \rho_i \left(\frac{\rho_i v_{m,i}^2}{\rho_i v_{s,i}^2 + \rho_i v_{c,i}^2} \right) \bigg/ \sum_{i=1}^{n} \rho_i, \qquad (4)$$

where m refers to the mode (solenoidal or compressive), ρ_i, $v_{s,i}$ and $v_{c,i}$ are the density, solenoidal velocity component and compressive velocity component of ith cell and n is the total number of cells. We calculate v_c and v_s at a uniform resolution of $\Delta x = 36.6\,\mathrm{pc}$ to ensure that the solenoidal motions are properly captured (i.e. $8 \times$ the width of a fully refined cell, as discussed in Renaud et al. 2015). First derivatives are computed using a stencil of ± 4 cells.

In Fig. 13, we show how f_s and f_c evolve as a function of time in our simulations. After an initial transient phase, the solenoidal modes become the dominate type of kinetic energy in all models; when feedback is not present, the solenoidal mode accounts for ~ 70 per cent of the turbulent energy budget, in good agreement with equipartition expectations. In the models with feedback, we find that solenoidal accounts for between 55 per cent and 66 per cent of the turbulent energy budget, meaning stellar feedback increases the importance of compressive (shock-dominated) turbulences. This is more significant in the larger MW model, whereas the effect is smaller in the dwarf galaxies, being almost negligible in the SMC model.

Despite the strong impact of feedback discussed in the previous sections, the simulations indicate that solenoidal motions dominate the turbulent energy budget. This suggests that energy and momentum injection related to feedback does not lead to compression-dominated ISM. Padoan et al. (2016) found that solenoidal motions could be produced by feedback as a result of expanding bubbles interacting with a non-uniform ISM through the baroclinic effect.

We also note that the fraction of energy in each component depends on scale: as Δx increases, and we hence probe gas motions on larger scales, we see an increase (decrease) in the fraction of kinetic energy found in the solenoidal (compressive) mode (see Fig. 13, bottom-left panel). Despite this dependence on scale, f_s is always >50 per cent and >66 per cent in feedback and no feedback simulations, respectively, i.e. independent of scale feedback always increases fraction of energy found in compressive modes.

4 DISCUSSION

4.1 Previous results from galaxy simulations

A number of studies have analysed the structure of the ISM using power spectra. Both Combes et al. (2012) and Walker et al. (2014) simulated MW-like galaxies including sub-grid models for stellar feedback. In agreement with our findings, both studies found that increasing the strength of feedback resulted in steeper H I density power spectra, fitted by single ($P \propto k^{-\alpha}$) or multiple power laws. Walker et al. (2014) found that models with weak feedback (their MUGS suite) featured shallow power laws ($\alpha \sim 1.2$) similar to $\alpha \sim 1.5$ found in our simulations without feedback. In their MaG-ICC suite of simulations, featuring significantly stronger feedback (SNe + 'early pre-SN' feedback), their recovered indices of $\alpha \sim 2.5$ closely match ours. However, in contrast to our models, they find that on scales $\ell \lesssim 2\,\mathrm{kpc}$, their spectra steepen considerably ($\alpha \sim 5$), in contrast to observed galaxies on those scales, as shown in Sec-

tion 3.2. The origin of this discrepancy may be that the MaGICC galaxies feature significantly thicker gaseous discs than analysed here, possibly due to the lower spatial resolution in those models ($\sim 155\,\mathrm{pc}$ compared to the 4.6 pc used here).

Bournaud et al. (2010) modelled an LMC-like galaxy to study the effect of feedback on the structure of the ISM. However, they found that their galaxies with and without feedback were both well fitted by two power laws, with a break at $\ell \sim 150\,\mathrm{pc}$, and with almost identical power-law indices on large ($\alpha \sim 1.9$) and small ($\alpha_{\mathrm{small}} = 3.12$) scales. Our LMC model is in excellent agreement with these values (see Fig. 4), but *only* when stellar feedback is present. As for the more massive galaxy models, we found that neglecting feedback resulted in shallower H I spectra, in contrast to the finding in Bournaud et al. (2010). It is unclear why our models give rise to such different conclusions, but we note that they adopt an equation of state for their ISM, instead of solving the full energy equation, which may stabilize the model without feedback enough to give rise to a structure compatible with their model including stellar feedback. Indeed, a visual inspection of their simulations (see figs 3 and 4 in Bournaud et al. 2010) reveals only small differences, mostly a slightly more porous ISM on small scales, with a large-scale morphology that does not resemble our fragmented LMC model when feedback is not present.

Pilkington et al. (2011) analysed dwarf galaxies formed in a cosmological context, and argued that single power-law fits to their models agreed with observations of similar mass galaxies such as the SMC. However, whereas the SMC indeed is well fitted by a single power law, their simulations are better fitted by multiple power laws with a break at $\sim 450\,\mathrm{pc}$. This is closer to what we find for our LMC and SMC simulations that include feedback, although the break occurs on smaller scales, and the exact values of the power-law indices in all of our models are larger, likely due to the definition of $\langle P(k) \rangle$, see discussion below.

Krumholz & Burkhart (2016) found that analytical models of feedback-driven turbulence predict a lower velocity dispersion for galaxies with an SFR $> 1\,\mathrm{M_\odot\,yr^{-1}}$ compared to gravity-only driven models (see their fig. 1). By comparing these models to observational data of gas velocity dispersion as a function of SFR, they argued that gravity is the primary source of turbulence in the ISM on scales typical of gravitational instabilities in galactic discs, i.e. supporting the conclusions of Goldbaum, Krumholz & Forbes (2016). Our simulations confirm this notion, where gravity-only models feature more kinetic energy than feedback-driven models on small scales ($\ell < h$). However, we emphasize that the role of feedback as a complementary driver of turbulence varies strongly with scale (as seen in Fig. 10), with large-scale power being of greater importance compared to gravity-only models.

We note however several caveats to their model that affect the interpretation of their results. The data set used to distinguish between gravity and feedback models has not been corrected for observational effects, difference in observational method or removal of rotational velocity. Instead, the raw observational data are used as reported by the authors. One example is the data from Lehnert et al. (2013) that used Hα lines to determine the velocity dispersion. These values are only corrected for resolution effects, i.e. rotation is not accounted for. Therefore, any results derived from these velocity dispersions are most likely an overestimate.

Furthermore, the models presented in Krumholz & Burkhart (2016) rely on the Toomre stability parameter for gas (Q_{g}), stars (Q_*) and the galaxy disc (Q), where $Q^{-1} = Q_*^{-1} + Q_{\mathrm{g}}^{-1}$ (see Toomre 1964; Wang & Silk 1994), assuming Q and Q_{g} to be equal to unity for the gravity and feedback models, respectively. We note
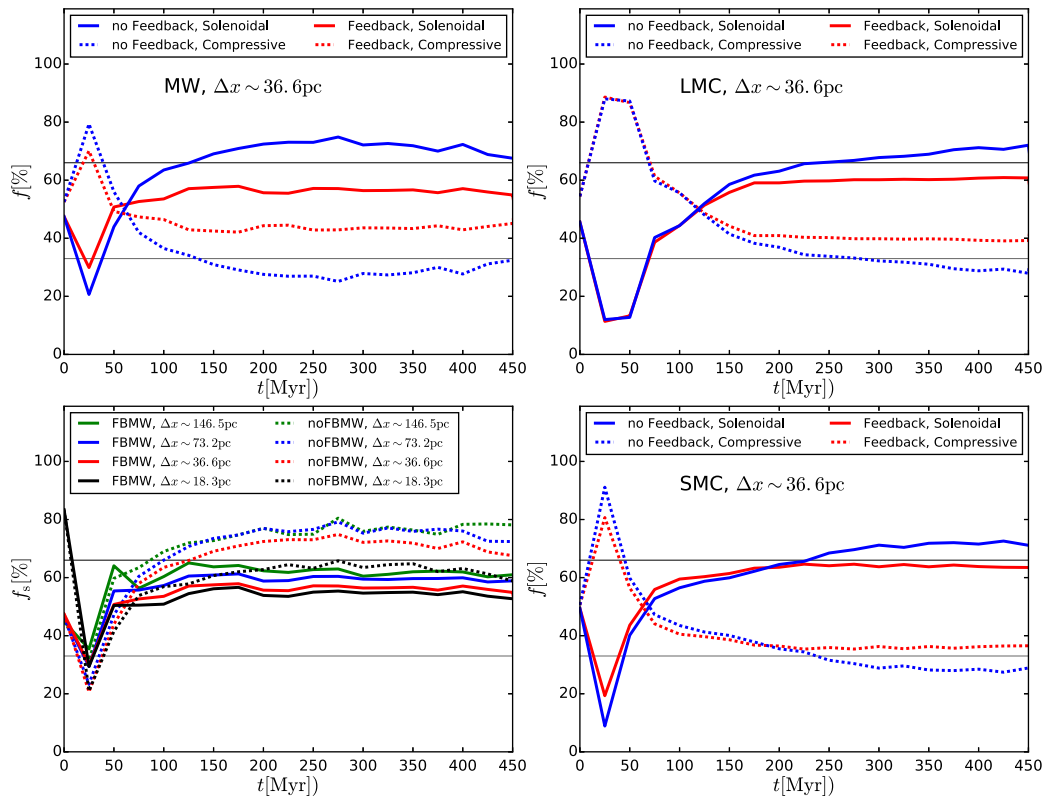
Figure 13. Top row and bottom right: mass-weighted fraction of turbulent kinetic energy in solenoidal (solid lines) and compressive (dashed lines) turbulent motion. Each panel shows the data for one set of simulations: the panel on the top left for the MW-like, the top-right panel shows the LMC-like and the bottom-right panel the SMC-like simulations. Simulations with feedback are shown with red lines while those without are shown with blue. We indicate the equipartition fractions with horizontal black ($f = 66$ per cent) and grey ($f = 33$ per cent) lines. Bottom left: comparison of the solenoidal fraction of our MW-like simulation when calculated at different resolutions (see the legend for resolution). Solid lines show results for the feedback run and dashed lines for no feedback.

that $Q = 1$ is a strong assumption. In fact, in the THINGS sample, star-forming spirals feature $Q \sim 1$–5 (see fig. 4 of Romeo & Falstad 2013), Q_g spans an even wider range of values (see fig. 5 of Romeo & Wiegert 2011), and both Q and Q_g depend on the scale over which they are measured (Hoffmann & Romeo 2012; Agertz et al 2015). All of the above can significantly affect the conclusions of Krumholz & Burkhart (2016).

4.2 Comparison with previous observational studies and caveats of our analysis

As discussed in Section 1, power spectrum analysis of the cold gas content of galaxies is common in the literature. In most, if not all, of these studies, the power spectra are well fitted by single or broken power laws from scales of a few 100 pc to kpc scales, in agreement with our analysis in Section 3.2. The power-law index for our sample of THINGS galaxies (NGC 628, 3521, 4736, 5055, 5457, 6946) matches the large-scale ($>$ few 100 pc) results recovered from our simulation of a MW-like spiral galaxy when feedback is present, with $\alpha \sim 2$–2.5. Without feedback, the spectra are too shallow to be compatible with observations.

We note that for four of the galaxies (NGC 628, 3521, 4736 and 5055), we find a larger value of α than those reported by Dutta et al. (2008, 2009a, 2013) and Dutta & Bharadwaj (2013) but a reasonable match to the indices quoted in Walker et al. (2014). A similar difference in power-law index was found for our SMC model, which featured an almost single power law with $\alpha = 1.8$, compared to the derived $\alpha = 2.85$ from observations (Stanimirovic

et al. 1999). In contrast to our findings, H I power spectra in local dwarf irregular galaxies in the little THINGS sample are found to be better fitted with steeper power laws (Zhang et al. 2012) compared to spiral galaxies (Dutta et al. 2013).

While it is tempting to discuss this, and other trends, further, we refrain from doing so as the value of the power-law index is known to depend on the adopted definition of the power spectrum, velocity channel width (Lazarian & Pogosyan 2000), integrated intensity maps versus single-velocity-channel maps (Padoan et al. 2006), etc., which differ significantly in the literature. For example, we have confirmed that our definition on $\langle P(k) \rangle$ agrees with Dutta et al. (2008, 2009a, 2013) and Dutta & Bharadwaj (2013, private communication), but find a difference in method; in this work, we have made use of the zeroth moment maps available from the THINGS data archive, while Dutta et al. (2008, 2009a, 2013) and Dutta & Bharadwaj (2013) calculate the *visibility*, defined as the Fourier transform of the sky brightness and then the power spectrum from this quantity. Recent work by Nandakumar & Dutta (in preparation) has demonstrated that using images from radio interferometry produces systematically *larger* values of α than a visibility-based method. They conclude that this difference is due to a noise bias that cannot easily be separated from the images and therefore any power spectrum from such a map would contain power from both the galaxy and noise.

To allow for a meaningful comparison between simulations and observations, it is important to analyse both in a similar way as possible, as was attempted in this work, but a complete homogenization of literature results is beyond the scope of this paper.

5 CONCLUSION

In this work, we study the role of stellar feedback in shaping the density and velocity structure of neutral hydrogen (H I) in disc galaxies. To achieve this, we use THINGS data to compute H I density and kinetic energy power spectra for six local spiral galaxies, and compare these to high-resolution ($\sim$4.6 pc) hydro+N-body simulations, using the AMR code RAMSES, of entire disc galaxies. We carry out simulations of MW-, LMC- and SMC-like galaxies, with and without stellar feedback, in order to identify differences in the ISM. Our key results are summarized below.

(i) Combined with gravity and shear, stellar feedback shapes the observed density field of galaxies, as illustrated through power spectra of H I gas. Feedback creates a steepening of the power spectra on spatial scales below $\sim$1$-$2 kpc, with $\alpha \sim 2.5$, in agreement with local spirals from THINGS. This match is achieved by feedback preventing regions of very high densities ($\rho > 10^4$ cm^{-3}) from dominating the density field, and instead allowing for star formation in gas of average densities $\rho \sim 100$ cm^{-3}, typical of observed GMCs of sizes $\sim$10-100 pc.

(ii) The large-scale shape of the H I power spectra ($\gtrsim$ few 1 kpc) is insensitive to stellar feedback and is controlled by the large-scale distribution of gas, i.e. the extent of H I at large galactic radii.

(iii) Line-of-sight H I kinetic energy power spectra ($E(k)$) from simulation with feedback are in good agreement with observations up to kpc scales for a majority of the studied spiral galaxies. Simulations without feedback underpredict the observed kinetic energy present on large scales ($\gtrsim$0.5 kpc), with excessive small-scale power due to the presence of dense star-forming clouds.

(iv) The inclination of a galaxy can have a significant impact on the measured line-of-sight H I kinetic energy power spectra of a galaxy, as the energy in galactic rotation dominates over turbulent energy. Correcting for this is crucial in order to use $E(k)$ to differentiate different feedback models. By contrast, the density power spectra are only weakly affected for the moderate inclination angles ($i \lesssim 40°$) investigated in this work.

(v) In 3D, simulations with feedback produce kinetic energy spectra $E(k) \propto k^{-2}$, as expected for supersonic turbulence, on scales $\lesssim$ few 100 pc, with a break at large scales possibly related to disc thickness. This can only be achieved if feedback acts as a mechanism for moving gas from the small to large scales, where it is then free to collapse down to small scales again. Without a mechanism such as feedback to redistribute gas, it accumulates at small to medium scales ($\ell \lesssim 300$ pc).

(vi) Without feedback, the ISM roughly reaches equipartition in terms of the fraction of kinetic energy in solenoidal motions (2/3) versus compressive (1/3). With stellar feedback, the fraction of energy in compressive modes increases to $\gtrsim$45 per cent for the MW model, with a similar trend, but weaker effect, in the SMC and LMC models.

To conclude, on top of gravity and shear, stellar feedback is a major driver of the density and energy structure of the ISM up to kpc scales, and these effects can be quantified using density and energy power spectra of H I gas.

Finally, despite omitted physics, such as magnetohydrodynamics, cosmological context and self-consistent modelling of H$_2$, we find a good agreement with observations, suggesting that these are next-to-leading order effects. We will revisit these areas in future work.

REFERENCES

Agertz O., Kravtsov A. V., 2015, ApJ, 804, 18
Agertz O., Kravtsov A. V., 2016, ApJ, 824, 79
Agertz O., Lake G., Teyssier R., Moore B., Mayer L., Romeo A. B., 2009, MNRAS, 392, 294
Agertz O., Kravtsov A. V., Leitner S. N., Gnedin N. Y., 2013, ApJ, 770, 25
Agertz O., Romeo A. B., Grisdale K., 2015, MNRAS, 449, 2156
Avila-Reese V., Colín P., González-Samaniego A., Valenzuela O., Firmani C., Velázquez H., Ceverino D., 2011, ApJ, 736, 134
Balbus S. A., Hawley J. F., 1991, ApJ, 376, 214
Belley J., Roy J. R., 1992, ApJS, 78, 61
Benson A. J., Bower R. G., Frenk C. S., Lacey C. G., Baugh C. M., Cole S., 2003, ApJ, 599, 38
Besla G., Kallivayalil N., Hernquist L., van der Marel R. P., Cox T., Keres D., 2010, ApJ, 721, L97
Bigiel F., Leroy A., Walter F., Brinks E., de Blok W. J. G., Madore B., Thornley M. D., 2008, AJ, 136, 2846
Block D., Puerari I., Elmegreen B., Bournaud F., 2010, ApJ, 718, L1
Blondin J. M., Wright E. B., Borkowski K. J., Reynolds S. P., 1998, ApJ, 500, 342
Bournaud F., Elmegreen B. G., Teyssier R., Block D. L., Puerari I., 2010, MNRAS, 409, 1088
Bullock J. S., Kolatt T. S., Sigad Y., Somerville R. S., Kravtsov A. V., Klypin A. A., Primack J. R., Dekel A., 2001, MNRAS, 321, 559
Burgers J., 1948, Adv. Appl. Mech., 1, 171
Chabrier G., 2003, PASP, 115, 763
Cioffi D. F., McKee C. F., Bertschinger E., 1988, ApJ, 334, 252
Combes F. et al., 2012, A&A, 539, A67
de Avillez M. A., Breitschwerdt D., 2004, A&A, 425, 899
de Avillez M. A., Breitschwerdt D., 2005, A&A, 436, 585
Dekel A., Silk J., 1986, ApJ, 303, 39
Dobbs C. L., Burkert A., Pringle J. E., 2011, MNRAS, 417, 1318
Dubois Y., Teyssier R., 2008, A&A, 477, 79
Dutta P., Bharadwaj S., 2013, MNRAS, 436, L49
Dutta P., Begum A., Bharadwaj S., Chengalur J. N., 2008, MNRAS, 384, L34
Dutta P., Begum A., Bharadwaj S., Chengalur J. N., 2009a, MNRAS, 397, L60
Dutta P., Begum A., Bharadwaj S., Chengalur J. N., 2009b, in Saikia D. J., Green D. A., Gupta Y., Venturi T., eds, ASP Conf. Ser. Vol. 407, The Low-Frequency Radio Universe. Astron. Soc. Pac., San Francisco, p. 83
Dutta P., Begum A., Bharadwaj S., Chengalur J. N., 2013, New Astron., 19, 89
Efstathiou G., 2000, MNRAS, 317, 697
Elmegreen B. G., Scalo J., 2004, ARA&A, 42, 211
Elmegreen B. G., Kim S., Staveley-Smith L., 2001, AJ, 548, 749
Federrath C., Klessen R. S., 2012, ApJ, 761, 156
Federrath C., Klessen R. S., 2013, ApJ, 763, 51
Federrath C., Roman-Duval J., Klessen R., Schmidt W., Mac Low M.-M., 2010, A&A, 512, A81
Frigo M., Johnson S. G., 2005, Proc. IEEE, 93, 216
Gammie C. F., Ostriker J. P., Jog C. J., 1991, ApJ, 378, 565

Gatto A., Fraternali F., Read J. I., Marinacci F., Lux H., Walch S., 2013, MNRAS, 433, 2749

Gatto A. et al., 2015, MNRAS, 449, 1057

Goldbaum N. J., Krumholz M. R., Forbes J. C., 2016, AJ, 827, 28

Guillet T., Teyssier R., 2011, J. Comput. Phys., 230, 4756

Hernquist L., 1990, ApJ, 356, 359

Hernquist L., 1993, ApJS, 86, 389

Hockney R. W., Eastwood J. W., 1981, Computer Simulation Using Particles. McGraw-Hill, New York

Hoffmann V., Romeo A. B., 2012, MNRAS, 425, 1511

Hopkins P. F., Quataert E., Murray N., 2012, MNRAS, 421, 3488

Hopkins P. F., Kereš D., Oñorbe J., Faucher-Giguère C. A., Quataert E., Murray N., Bullock J. S., 2014, MNRAS, 445, 581

Ibáñez-Mejía J. C., Mac Low M.-M., Klessen R. S., Baczynski C., 2016, ApJ, 824, 41

Joung M. K. R., Mac Low M.-M., 2006, ApJ, 653, 1266

Katz N., 1992, ApJ, 391, 502

Kennicutt R. C., Jr, 1998, AJ, 498, 541

Kennicutt R. C., Jr, Hodge P. W., 1986, AJ, 306, 130

Kessel-Deynet O., Burkert A., 2003, MNRAS, 338, 545

Kim C. G., Ostriker E. C., 2015, AJ, 802

Kim S., Staveley-Smith L., Dopita M. A., Freeman K. C., Sault R. J., Kesteven M. J., McConnell D., 1998, ApJ, 503, 674

Kim J., Balsara D., Mac Low M. M., 2001, J. Korean Astron. Soc., 34, 333

Kim J. h. et al., 2014, ApJS, 210, 14

Kimm T., Cen R., Devriendt J., Dubois Y., Slyz A., 2015, MNRAS, 451, 2900

Klypin A., Prada F., 2009, ApJ, 690, 1488

Kolmogorov A., 1941, Dokl. Akad. Nauk SSSR, 30, 301

Kravtsov A. V., 2003, ApJ, 590, L1

Kravtsov A., Vikhlinin A., Meshscheryakov A., 2014, ApJ, preprint (arXiv:1401.7329)

Kritsuk A. G., Norman M. L., Padoan P., Wagner R., 2007a, ApJ, 665, 416

Kritsuk A. G., Padoan P., Wagner R., Norman M. L., 2007b, in AIP Conf. Ser. Vol. 932, Turbulence and Nonlinear Processes in Astrophysical Plasmas. Am. Inst. Phys., New York, p. 393

Krumholz M. R., Burkhart B., 2016, MNRAS, 458, 1671

Krumholz M. R., Tan J. C., 2007, ApJ, 654, 304

Krumholz M. R., McKee C. F., Tumlinson J., 2008, ApJ, 689, 865

Krumholz M. R., McKee C. F., Tumlinson J., 2009, AJ, 699, 850

Larson R. B., 1981, MNRAS, 194, 809

Lazarian A., Pogosyan D., 2000, ApJ, 537, 720

Lehnert M. D., Tiran L. L., Nesvadba N. P. H., van Driel W., Boulanger F., Matteo P. D., 2013, A&A, 555, 18

Leroy A. K. et al., 2009, AJ, 137, 4670

Licquia T. C., Newman J. A., 2015, AJ, 806, 20

Mac Low M. M., Klessen R. S., 2004, Rev. Mod. Phys., 76, 125

McKee C. F., Ostriker E. C., 2007, ARA&A, 45, 565

Mandelbaum R., Seljak U., Kauffmann G., Hirata C. M., Brinkmann J., 2006, MNRAS, 368, 715

Marasco A., Debattista V. P., Fraternali F., van der Hulst T., Wadsley J., Quinn T., Roškar R., 2015, MNRAS, 451, 4223

Martin P., Belley J., 1997, A&A, 321, 363

Martizzi D., Faucher-Giguere C. A., Quataert E., 2015, MNRAS, 450, 504

Martizzi D., Fielding D., Faucher-Giguere C. A., Quataert E., 2016, MNRAS, 459, 2311

Meatheringham S. J., Dopita M. A., Ford H. C., Webster B. L., 1988, ApJ, 327, 651

Meurer G. R., 1994 in Meylan G., Prugniel P. eds., 1994, Dwarf Galaxies. ESO, Garching, p. 351

Meurer G. R., Carignan C., Beaulieu S. F., Freeman K. C., 1996, AJ, 111, 1551

Mo H., Mao S., White S. D., 1998, MNRAS, 295, 319

More S., van den Bosch F. C., Cacciato M., Skibba R., Mo H. J., Yang X., 2011, MNRAS, 410, 210

Murray N. W., Rahman M., 2010, AJ, 709, 424

Navarro J. F., White S. D. M., 1993, MNRAS, 265, 271

Navarro J. F., Frenk C. S., White S. D. M., 1996, ApJ, 462, 563

Nordlund A., Padoan P., 1999, in Franco J., Carraminana A., eds, Proceedings of the 2nd Guillermo Haro Conference, Interstellar Turbulence. Cambridge Univ. Press, Cambridge, p. 218

Oosterloo T., Morganti R., Sadler E., van der Hulst J., Serra P., 2007, A&A, 465, 787

Padoan P., Nordlund A., Jones B. J. T., 1997, MNRAS, 288, 145

Padoan P., Kim S., Goodman A., Staveley-Smith L., 2001, ApJ, 555, L33

Padoan P., Juvela M., Kritsuk A., Norman M. L., 2006, ApJ, 653, L125

Padoan P., Federrath C., Chabrier G., Evans N. J., II, Johnstone D., Jørgensen J. K., McKee C. F., Nordlund Å., 2014, in Beuther H., Klessen R. S., Dullemond C. P., Henning Th., eds, Protostars and Planets VI. Univ. Arizona Press

Padoan P., Pan L., Haugboelle T., Nordlund A., 2016, AJ, 822, 11

Pilkington K. et al., 2011, MNRAS, 417, 2891

Piontek R. A., Ostriker E. C., 2004, ApJ, 601, 905

Planck Collaboration XIII, 2016, A&A, 594, A13

Read J. I., Trentham N., 2005, Phil. Trans. R. Soc. A, 363, 2693

Read J. I., Agertz O., Collins M. L. M., 2016a, MNRAS, 459, 2573

Read J. I., Iorio G., Agertz O., Fraternali F., 2016b, preprint (arXiv:1607.03127)

Read J. I., Iorio G., Agertz O., Fraternali F., 2016c, MNRAS, 462, 3628

Renaud F. et al., 2013, MNRAS, 436, 1836

Renaud F., Bournaud F., Kraljic K., Duc P. A., 2014, MNRAS, 442, L33

Renaud F. et al., 2015, MNRAS, 454, 3299

Riley K. F., Hobson M. P., Bence S. J., 2006, Mathematical Methods for Physics and Engineering, 3rd edn. Cambridge Univ. Press, Cambridge

Robertson B. E., Kravtsov A. V., 2008, ApJ, 680, 1083

Rogstad D. H., Lockhart I. A., Wright M. C. H., 1974, ApJ, 193, 309

Romeo A. B., Agertz O., 2014, MNRAS, 442, 1230

Romeo A. B., Falstad N., 2013, MNRAS, 433, 1389

Romeo A. B., Fathi K., 2015, MNRAS, 451, 2107

Romeo A. B., Wiegert J., 2011, MNRAS, 416, 1191

Romeo A. B., Agertz O., Moore B., Stadel J., 2008, ApJ, 686, 1

Romeo A. B., Burkert A., Agertz O., 2010, MNRAS, 407, 1223

Scannapieco C. et al., 2012, MNRAS, 423, 1726

Scott T. C. et al., 2014, A&A, 567, A56

Silk J., Rees M. J., 1998, A&A, 331, L1

Simpson C. M., Bryan G. L., Hummels C., Ostriker J. P., 2015, AJ, 809, 69

Skibba R. A. et al., 2011, ApJ, 738, 89

Springel V., 2000, MNRAS, 312, 859

Springel V., Di Matteo T., Hernquist L., 2005, MNRAS, 361, 776

Stanimirovic S., Staveley-Smith L., Dickey J. M., Sault R. J., Snowden S. L., 1999, MNRAS, 302, 417

Stanimirovic S., Staveley-Smith L., Jones P., 2004, AJ, 604, 176

Stinson G., Seth A., Katz N., Wadsley J., Governato F., Quinn T., 2006, MNRAS, 373, 1074

Stinson G. S., Brook C., Macciò A. V., Wadsley J., Quinn T. R., Couchman H. M. P., 2013, MNRAS, 428, 129

Tamburro D., Rix H. W., Leroy A. K., Mac Low M. M., Walter F., Kennicutt R. C., Brinks E., de Blok W. J. G., 2009, AJ, 137, 4424

Tasitsiomi A., Kravtsov A. V., Wechsler R. H., Primack J. R., 2004, ApJ, 614, 533

Tasker E. J., Bryan G. L., 2006, ApJ, 641, 878

Teodoro E. D., Fraternali F., 2015, MNRAS, 451, 3021

Teyssier R., 2002, A&A, 385, 337

Thacker R. J., Couchman H. M. P., 2001, ApJ, 555, L17

Thornley M. D., 1996, AJ, 469, L45

Thornton K., Gaudlitz M., Janka H. T., Steinmetz M., 1998, ApJ, 500, 95

Toomre A., 1964, ApJ, 139, 1217

Vale A., Ostriker J. P., 2004, MNRAS, 353, 189

van der Marel R. P., Alves D. R., Hardy E., Suntzeff N. B., 2002, AJ, 124, 2639

Vazquez-Semadeni E., 1994, AJ, 423, 681

Wada K., Norman C. A., 2001, AJ, 546, 172

Wada K., Norman C. A., 2007, ApJ, 660, 276

Wada K., Meurer G., Norman C. A., 2002, ApJ, 577, 197

Walch S. et al., 2015, MNRAS, 454, 238

Walker A., Gibson B., Pilkington K., Brook C., Dutta P., Stanimirovic S., Stinson G., Bailin J., 2014, MNRAS, 441, 525

Walter F., Brinks E., de Blok W., Bigiel F., Kennicutt R. C., Jr, Thornley M., Leroy A., 2008, AJ, 136, 2563

Wang B., Silk J., 1994, ApJ, 427, 759

Whitney B. A. et al., 2008, AJ, 136, 18

Wilke K., Klaas U., Lemke D., Mattila K., Stickel M., Haas M., 2004, A&A, 414, 69

Yozin C., Bekki K., 2014, MNRAS, 443, 522

Zhang H. X., Hunter D. A., Elmegreen B. G., 2012, ApJ, 754, 29

This paper has been typeset from a TeX/LaTeX file prepared by the author.